*mining*

MDPI

*Article*

# Compressed $CO_2$ Energy Storage in Southern Ontario: Plume-Dynamics and Geomechanics Analyses

**Jingyu Huang [1], Yutong Chai [1,*], Jennifer Williams [2] and Shunde Yin [1,*]**

[1] Department of Civil and Environmental Engineering, University of Waterloo, Waterloo, ON N2l 3Gl, Canada; j583huang@uwaterloo.ca
[2] Newfoundland and Labrador Hydro, St John's, NL A1B 4K7, Canada; jenniferwilliams@nlh.nl.ca
* Correspondence: y5chai@uwaterloo.ca (Y.C.); shunde.yin@uwaterloo.ca (S.Y.)

**Abstract**

Compressed $CO_2$ energy storage (CCES) in deep sedimentary basins offers a promising option to integrate carbon management with long-duration energy storage. However, most existing subsurface energy-storage studies focus on salt caverns or generic porous reservoirs, while the potential of evaporite-bounded carbonate reservoirs remains insufficiently explored. This study presents the first application-oriented numerical assessment of CCES in Southern Ontario. It investigates the feasibility of CCES in the Upper Silurian Salina Group beneath offshore Lake Huron, focusing on a porous A-2 carbonate interval vertically confined by B and A-2 halite caprocks. A fully coupled three-dimensional thermo-hydro-mechanical model is developed in COMSOL Multiphysics 6.3 to simulate two-phase (brine-$CO_2$) Darcy flow, heat transfer, and poroelastic deformation under a realistic Michigan Basin stress, pressure and geothermal regime. After an initial cushion-gas stage at 8 kg/s that establishes a caprock-parallel supercritical $CO_2$ wedge beneath the B-salt, 24 h injection-production cycles are imposed for two years, followed by a five-month high-resolution window. Three well completion strategies are compared: full-length, upper-only, and split (upper + lower) perforations. Results indicate that in all simulations the $CO_2$ plume stabilizes as a persistent gas cap beneath the B-salt, far-field pressures remain close to hydrostatic, and reservoir deformations are very small, pointing to a substantial geomechanical safety margin. Among the three completion strategies, the split completion provides the best compromise: it maintains high and relatively stable $CO_2$ production while avoiding the stronger lower-zone depressurisation seen in the full-length case and the more limited working volume of the upper-only case. These findings suggest that a Salina A-2 carbonate reservoir bounded by B and A-2 salts can accommodate cyclic CCES under realistic basin conditions, and that appropriately designed split completions offer a practical balance between storage utilisation and operational robustness in this setting.

**Keywords:** porous-media $CO_2$ storage; compressed $CO_2$ energy storage; Salina Group; thermo-hydro-mechanical coupling

Check for updates

Academic Editor: Mostafa Benzaazoua

Received: 26 March 2026
Revised: 30 April 2026
Accepted: 5 May 2026
Published: 14 May 2026

**Copyright:** © 2026 by the authors. Licensee MDPI, Basel, Switzerland. This article is an open access article distributed under the terms and conditions of the Creative Commons Attribution (CC BY) license.

## 1. Introduction

Anthropogenic greenhouse gas emissions have been identified as the dominant driver of contemporary climate change, with $CO_2$ representing the largest contribution to radiative forcing among long-lived greenhouse gases [1]. Long-term atmospheric observations show that $CO_2$ concentrations have continued to rise since the pre-industrial period, with recent assessments confirming that this persistent increase is predominantly driven by fossil fuel

combustion and industrial processes [2]. Rising atmospheric $CO_2$ concentrations have driven a clear increase in global mean surface temperature, with anthropogenic warming reaching about 1.1 °C relative to pre-industrial conditions, and have substantially increased the occurrence and intensity of extreme events such as heatwaves, droughts, and intense precipitation worldwide [3].

Recent mitigation analyses consistently indicate that deep reductions in $CO_2$ emissions alone are insufficient to achieve long-term climate stabilization, and carbon capture and storage (CCS) plays a critical role in net-zero and low-temperature-rise pathways, particularly for hard-to-abate sectors such as power generation, cement, steel, and chemical industries [4–6]. Integrated assessment and techno-economic studies further demonstrate that excluding CCS significantly increases system costs and limits feasible decarbonization pathways, highlighting its role as a complementary option to renewable energy and electrification [5].

Among available CCS options, geological storage of $CO_2$ in deep subsurface formations including saline aquifers, depleted hydrocarbon reservoirs, and evaporite-sealed systems has been widely recognized as the only technically viable solution for permanent $CO_2$ sequestration at the gigaton scale. Recent assessments emphasize that global sedimentary basins possess sufficient storage capacity to accommodate cumulative $CO_2$ emissions over multi-decadal timescales, provided that appropriate site selection, pressure management, and monitoring strategies are implemented [7,8].

Beyond mitigating climate change through large-scale carbon sequestration, deep decarbonization of the energy system itself is another focus to effectively limit global warming. Numerous energy system analyses have demonstrated that rapid deployment of low-carbon electricity generation, particularly wind and solar power, is a cornerstone of emission reduction strategies, as it directly displaces fossil fuel-based power generation and reduces long-term $CO_2$ emissions from the energy sector [9,10]. As a result, global electricity systems are increasingly transitioning toward power mixes dominated by renewable energy sources with near-zero operational emissions.

However, the large-scale integration of wind and solar energy introduces substantial operational challenges due to their inherent variability and limited dispatchability. Recent studies consistently show that high penetration of variable renewable energy leads to pronounced temporal mismatches between electricity supply and demand, increasing the need for system flexibility across hourly, daily, and seasonal timescales [11–13]. Consequently, achieving reliable and low-carbon power systems with high shares of renewables requires the deployment of large-scale, long-duration energy storage technologies capable of balancing power generation and consumption over extended periods [14]. However, existing energy storage technologies exhibit distinct limitations when extended from short-duration to multi-day or seasonal applications. Electrochemical batteries, while effective for short-term balancing, face challenges related to cost, material availability, and degradation when deployed at the scales required for long-duration storage, whereas pumped hydro storage is strongly constrained by geographical and topographical conditions [12,14].

These limitations have motivated increasing interest in geological and subsurface energy storage concepts, which exploit the large storage capacity, pressure tolerance, and thermal inertia of underground formations to provide scalable and cost-effective long-duration energy storage solutions with minimal surface footprint [15–17]. Within this class of technologies, compressed gas energy storage has attracted sustained attention due to its high energy density and compatibility with a wide range of geological settings.

Building upon the growing interest in subsurface energy storage, compressed carbon dioxide energy storage (CCES) has recently emerged as a promising alternative to conventional compressed gas concepts. Compared with air, carbon dioxide exhibits a

substantially higher density and compressibility near and above its critical point (31.1 °C, 7.38 MPa), enabling significantly higher energy storage density under geological pressure conditions achievable at moderate depths [18,19]. When injected into deep geological formations, $CO_2$ can be maintained in a supercritical state, combining gas-like mobility with liquid-like density, which enhances storage efficiency and improves injectivity in subsurface reservoirs [18].

In addition, recent studies have highlighted the potential of integrating CCES with subsurface thermal resources, where geothermal gradients and formation heat can be exploited to partially offset compression losses and improve round-trip efficiency. Such thermo-mechanical coupling allows stored $CO_2$ to act simultaneously as an energy carrier and a heat-transfer fluid, offering new opportunities for improving the overall performance of underground energy storage systems [18–20].

Building on this concept, this study investigates CCES in porous media within the Salina Group of the Michigan Basin, with a particular focus on potential application in the deep, high-pressure offshore domain beneath Lake Huron on the Ontario side. The Michigan Basin contains laterally continuous, gently dipping Salina Group strata with thick evaporite successions. At depths greater than approximately 800–1000 m, these units provide mechanically competent caprocks and favourable pressure containment [21–24]. These conditions enable injected $CO_2$ to be maintained in a dense or supercritical state under realistic geological constraints, supporting pressure-controlled cyclic injection and production [25,26]. In contrast to $CO_2$-based geothermal concepts that seek to extract substantial heat, the present study focuses on pressure-driven compressed $CO_2$ energy storage, where formation temperature plays only a supporting role. Under the moderate geothermal conditions expected in the target area, subsurface heat is considered primarily as a thermal buffer that helps maintain supercritical $CO_2$ during cyclic operation, rather than as an additional energy source.

Previous work on onshore Lambton County and the Sarnia-Windsor corridor has already demonstrated the suitability of the Salina B and A-2 salts for cavern-based storage of hydrocarbons and hydrogen, emphasizing their mechanical competence, low permeability and long-term operational performance as regional seals [26–28]. Building on this evaporite framework, the present study instead treats the A-2 carbonate interval between the B and A-2 salts as a porous-media reservoir for compressed $CO_2$ energy storage, with the over- and underlying halite bodies providing vertical confinement. This represents a new application of the Salina Group storage system in Southern Ontario, shifting the target from solution-mined salt caverns to an evaporite-confined carbonate reservoir for cyclic CCES. By explicitly linking system design to a realistic stratigraphic and depth configuration beneath offshore Lake Huron, the study conducts a comparative optimisation of cyclic injection-production strategies for compressed $CO_2$ within this saline evaporite-carbonate succession, shifting the focus from generic cavern-based concepts to a site-specific, basin-scale operational design for CCES in the Salina Group. This site-specific framework allows plume evolution, pressure cycling, thermal response, and geomechanical deformation to be evaluated together, providing a more integrated basis for assessing CCES feasibility and completion performance than generic storage concepts.

## 2. Geological Setting

Southern Ontario occupies the eastern flank of the Michigan Basin, a broad, nearly circular intracratonic basin that developed during the Paleozoic and contains more than 4–5 km of sedimentary strata in its depocenter. Within this succession, the Upper Silurian Salina Group represents a major evaporitic interval deposited during a period of restricted marine circulation. The Salina Group forms a regionally extensive evaporite-

carbonate succession that locally attains several hundred metres in thickness across the basin. Stratigraphic studies subdivide the unit into a stacked A–H sequence, reflecting repeated evaporative cycles under shallow marine to sabkha conditions. These cycles produced thick halite-dominated intervals interbedded with dolomite, anhydrite, and minor shale, recording fluctuations in salinity, water depth, and basin connectivity [25,26]. Figure 1 demonstrates the subdivision of the Salina Formation.

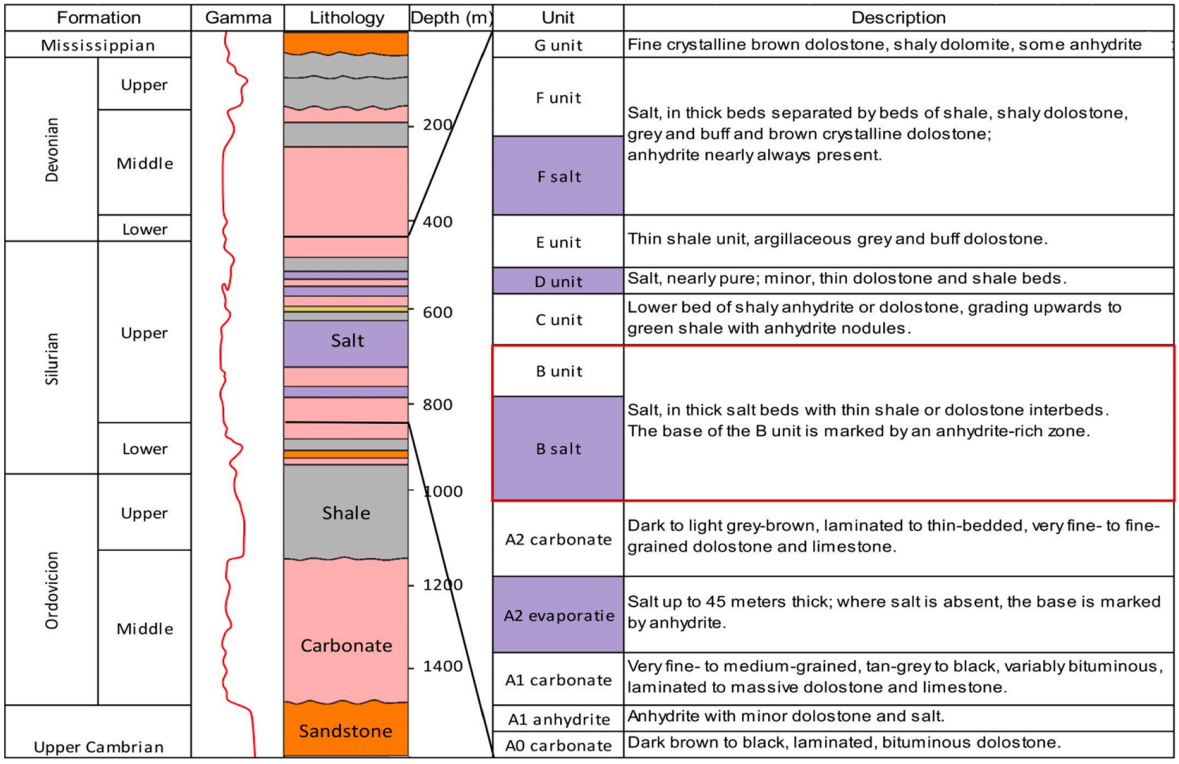


**Figure 1.** Stratigraphic subdivision of the Salina Formation. Colours denote lithological units, and the red box highlights the Salina B unit considered as the upper sealing layer in this study [28].

In the eastern basin and offshore sector beneath Lake Huron, the Salina Group remains gently dipping (typically <1–2°) and structurally simple, with only broad, kilometre-scale warping and minor faulting. Regional mapping and analyses of evaporite architecture indicate that the cumulative thickness of Salina evaporites, including salt, gypsum, and anhydrite, commonly exceeds 200–400 m where salt beds occur at depths shallower than approximately 1000–1200 m. Along the Ontario-Michigan border, the total evaporite thickness may locally exceed 350–400 m [22,23]. These studies also highlight the persistence of bedded salt panels suitable for underground storage, with limited evidence of deep dissolution away from basin margins, implying favorable hydrologic isolation of the deeper salt sequence [23].

Within this framework, the present study focuses on the Salina B and A-2 units in the offshore Ontario sector of the Michigan Basin, where these evaporites and associated carbonates form a vertically stacked caprock-reservoir-caprock system. Regional seismic and well interpretations demonstrate that the Salina B unit is dominated by massive to bedded halite with subordinate anhydrite and dolomite, and locally attains thicknesses of 60–100 m [29]. Below B, the A-1 interval is typically developed as an evaporite-carbonate composite, while the A-2 subunits comprise an upper carbonate member (A-2 carbonate) and a lower halite-rich evaporite (A-2 salt). High-resolution stratigraphic work in the Michigan Basin indicates that the A-2 interval includes a carbonate member with dolomitized and moderately porous facies that can host injected fluids, while the overlying B salt and

underlying A-2 evaporite form laterally extensive, low-permeability halite units that act as regional upper and lower seals [25,26].

On this basis, the B–A-1–A-2 succession beneath offshore Lake Huron is treated as a representative evaporite-bounded reservoir system. The B and A-2 salts provide vertical confinement for the porous A-2 carbonate interval. This simplified but geologically constrained framework forms the basis for the numerical models developed in the following sections, where pressure-driven CCES scenarios and cyclic injection-production strategies are evaluated.

## 3. Constitutive Model

### *3.1. Two-Phase Flow of Brine and $CO_2$ in Porous Media*

Flow in the A-2 carbonate is represented as two-phase Darcy flow of a wetting brine phase (w) and a non-wetting $CO_2$ phase (n). The initial hydraulic state of the A-2 carbonate is assumed to be fully water-saturated. This choice reflects the likely conditions in a deep, offshore saline formation beneath Lake Huron, where the reservoir has not been previously invaded by hydrocarbons and is expected to be originally saturated with formation brine. In a prospective development scenario, the reservoir could be pre-conditioned by stimulation treatments such as acidizing to enhance permeability and connectivity. However, these treatments would not change the basic initial condition that $CO_2$ is injected into a brine-filled pore space. The phase saturations satisfy:

$$S_w + S_n = 1 \tag{1}$$

For each phase $i \in \{w, n\}$, the mass conservation equation is

$$\frac{\partial \varnothing \rho_i S_i}{\partial t} + \nabla(\rho_i u_i) = Q_{S_i} \tag{2}$$

where $\varnothing$ is porosity, $\rho_i$ is density, $u_i$ is the Darcy velocity, and $Q_{S_i}$ represents distributed sources due to injection and production.

For both the brine and $CO_2$ phases, fluid flow was described using Darcy's law. Because injection and production occur within a porous carbonate reservoir, flow velocities are low and the Reynolds number remains within the laminar regime. Thus, inertial effects are negligible, and Darcy's law is appropriate for describing flow through the porous medium.

The Darcy velocity for brine and supercritical $CO_2$ is defined as

$$u_i = -\frac{\kappa}{\mu_i}(\nabla p_f - \rho_i g) \tag{3}$$

with $\kappa$ the permeability of rock mass, $\mu$ the dynamic viscosity, $p_f$ the pore pressure, and $g$ gravitational acceleration. The host rock is assumed isotropic.

A volume-averaged mass balance over a representative elementary volume links the Darcy flow and phase transport formulations. At accumulative scale, the governing equation can be written as:

$$\frac{\partial \varnothing \overline{\rho}}{\partial t} + \nabla \overline{\rho}\,\overline{u} = \sum_i Q_{S_i} \tag{4}$$

where

$$\overline{u} = -\frac{\kappa}{\overline{\mu}}(\nabla p_f - \overline{\rho} g) \tag{5}$$

$$\overline{\mu} = \frac{\overline{\rho}}{\sum_i \frac{\kappa_{rs_i}\rho_i}{\mu_i}} \tag{6}$$

$$\overline{\rho} = \sum_{i} \rho_i S_i \tag{7}$$

Here $\kappa_{rs_i}$ is the relative permeability for the two phases. In the two-phase flow model, capillary pressure and relative permeability are represented using a Brooks-Corey formulation. The water and gas saturations $S_w$ and $S_n$ are first converted to effective saturations $\overline{S_w}$ and $\overline{S_n}$ by removing the residual saturations $S_{rw}$ and $S_{rn}$ and normalizing by the mobile saturation range. These two parameters can be written as:

$$\overline{S_n} = \frac{S_n - S_{rn}}{1 - S_{rw} - S_{rn}} \tag{8}$$

$$\overline{S_w} = \frac{S_w - S_{rw}}{1 - S_{rw} - S_{rn}} \tag{9}$$

The residual saturations for brine and supercritical $CO_2$ are 0.2 and 0.05, respectively. Capillary pressure is then expressed as:

$$P_c = P_{ec} \overline{S_w}^{\frac{-1}{\lambda_p}} \tag{10}$$

where $P_{ec} = 10$ KPa is the entry capillary pressure and $\lambda_p = 2$ is the pore-size distribution index. The relative permeabilities of the wetting and non-wetting phases are given by Corey-type power laws of the effective saturations:

$$\kappa_{rs_n} = \overline{S_n}^2 (1 - (1 - \overline{S_n})^{1 + \frac{2}{\lambda_p}}) \tag{11}$$

$$\kappa_{rs_w} = \overline{S_w}^{3 + \frac{2}{\lambda_p}} \tag{12}$$

### *3.2. Thermo-Poroelastic Constitutive Model*

In this study, the rock matrix including salt and carbonates is treated as a linear, isotropic, thermo-poroelastic continuum. The small-strain tensor is decomposed as:

$$\varepsilon = \varepsilon^e + \varepsilon^{th} \tag{13}$$

where $\varepsilon^e$ is the elastic strain and $\varepsilon^{th}$ is the thermal strain.

The thermal strain term is given by

$$\varepsilon_{th} = \alpha (T - T_{ref}) I \tag{14}$$

where $\alpha$ is the coefficient of thermal expansion of the rock, T is temperature, $T_{ref}$ denotes reservoir reference temperature, and I is the second order identity tensor.

Biot's poroelasticity theory was employed to capture the coupling between solid deformation and overall pore pressure evolution in the two-phase system during compressed $CO_2$ injection. The equilibrium equation can be expressed as follows [29]:

$$\nabla \cdot (S - \alpha_B P_f I) + f_V = 0 \tag{15}$$

where S is the total stress tensor, $P_f$ is the pore pressure, $\alpha_B$ is the Biot coefficient, and $f_V$ is the body force vector.

The fluid mass balance is written as [29]:

$$\overline{\rho} s_p \frac{\partial P_f}{\partial t} + \nabla \overline{\rho} \overline{u} = -\overline{\rho} \alpha_B \frac{\partial \varepsilon_{vol}}{\partial t} + Q_m \tag{16}$$

where $\overline{\rho}$ is the average fluid density, $\overline{u}$ is the average Darcy velocity, and $\varepsilon_{vol}$ is the volumetric strain of the solid skeleton. In the absence of inelastic deformation, this volumetric strain is simply the trace of the elastic strain tensor. $Q_m$ is a source term. The storage coefficient is defined as:

$$s_p = \varepsilon_p \chi_f + (\alpha_B - \varepsilon_p)\chi_s \tag{17}$$

with $\chi_f$ the fluid compressibility, and $\chi_s$ the solid compressibility, expressed as:

$$\chi_s = \frac{1 - \alpha_B}{K_d} \tag{18}$$

where $K_d$ is the drained bulk modulus of the porous medium.

### *3.3. Heat Transfer in Porous Media*

Heat transfer in the reservoir is formulated by applying a control-volume energy balance to the coupled rock-fluid system. Starting from the first law of thermodynamics for a representative elementary volume, kinetic and potential energy terms are neglected, no shaft work is considered, and pressure work is treated implicitly through the Darcy-flow formulation. These modeling assumptions are reasonable for the present problem as flow in the A-2 carbonate occurs at low velocities, so changes in kinetic energy are negligible compared with sensible heat stored in the rock-fluid system. The vertical and lateral pressure gradients are modest and the model domain is relatively compact, making gravitational potential energy changes small relative to thermal effects. Under these assumptions, the only explicit heat interactions are conduction and enthalpy advection by the pore fluid. Combining both solid matrix (subscript s) and pore fluid (subscript f) energy balances under the assumption of local thermal equilibrium, a single effective energy equation of the form is simplified as below:

$$(\rho C_p)_{eff} \frac{\partial T}{\partial t} + \rho_f C_{p,f} \overline{u} \nabla T - \nabla \cdot (\lambda_{eff} \nabla T) = Q \tag{19}$$

where Q is the total heat source, $(\rho C_p)_{eff}$ is the effective volumetric heat capacity of the saturated medium, $\rho_f C_{p,f}$ is the effective volumetric heat capacity of the fluid, and $\lambda_{eff}$ is the effective thermal conductivity. These are defined as follows:

$$\rho_f C_{p,f} = \sum_i \rho_i S_i C_{p,i} \tag{20}$$

$$(\rho C_p)_{eff} = (1 - \varnothing)\rho_s C_{p,s} + \varnothing \rho_f C_{p,f} \tag{21}$$

$$\lambda_{eff} = (1 - \varnothing)\lambda_s + \varnothing \lambda_f \tag{22}$$

## 4. Numerical Model

A three-dimensional thermo-hydro-mechanical model was built in COMSOL Multiphysics 6.3 to simulate compressed $CO_2$ energy storage in the Salina Group beneath the offshore Ontario sector of the Michigan Basin. The modeled sequence is simplified to three laterally continuous layers: an upper B salt caprock as upper sealing caprock, a porous A-2 carbonate reservoir, and a lower A-2 evaporite bedrock. Based on regional thickness data for southwestern Ontario, the B salt is assigned a representative thickness of 80 m, the A-2 carbonate 40 m, and the A-2 salt 40 m [30]. To represent deeper burial toward the basin axis beneath Lake Huron and maintain supercritical $CO_2$ conditions, the reservoir is placed below approximately 800 m. Accordingly, the entire B–A-2 sequence is assigned a representative depth configuration corresponding to the deeper offshore sector beneath Lake Huron: the top of the B salt lies 900 m below the lake surface, the A-2 carbonate reservoir

spans 980–1020 m, and the underlying A-2 salt forms a lower caprock between 1020 and 1060 m depth. This depth range is consistent with regional compilations showing total Paleozoic thicknesses exceeding 1.5 km in the offshore sector and Salina sub-units occurring at depths > 0.8–1.0 km [30]. The model domain extends 700 m × 700 m to minimise boundary effects from injection-production cycles. The stratigraphy is simplified as horizontal and laterally uniform, consistent with the gentle dip and simple structural setting of the Salina Group in the eastern Michigan Basin and offshore Lake Huron [25]. The vertical well is represented as a 1D line feature perforated only across the A-2 carbonate; and is operated in cyclic injection-production mode with time-dependent mass-flow boundary conditions. Following common practice in gas storage and $CO_2$ injection well design, the perforated interval is restricted to the central A-2 carbonate. A 5 m unperforated buffer is retained below the B salt and above the A-2 salt to protect the caprocks and reduce the influence of low-permeability halite on well injectivity. The overlying B salt and underlying A-2 salt are composed of very low-permeability halite, which acts as an effective caprock for gas and $CO_2$ storage. Accordingly, $CO_2$ leakage into the evaporite units was neglected, and fluid flow was simulated only within the A-2 carbonate reservoir [31,32]. Consistent with the hydrostatic pressure initialization, the lateral boundaries of the A-2 carbonate reservoir were assigned hydrostatic pressure conditions using the Lake Huron water surface as the reference hydraulic head.

Material properties for the rock formations were compiled from laboratory and field data on Salina bedded salts and carbonates in southern Ontario and comparable North American salt provinces [26,27,33,34]. In the absence of site-specific core tests for the offshore Lake Huron sector, these published ranges are used to select single representative values for each layer, rather than attempting detailed spatial variability. Reported A-2 carbonate permeabilities are generally modest. Here, a higher effective permeability is assumed to represent a reasonably enhanced flow-capacity scenario after potential pre-treatment, such as acidizing or stimulation. The selected permeability of $1 \times 10^{-13}$ $m^2$ is within the lower range of permeabilities commonly regarded as good-quality reservoir rocks. It is therefore treated as an assumed effective permeability representing a reasonably enhanced flow-capacity scenario, rather than a directly measured in situ value for the offshore A-2 carbonate.

The detailed properties of the rock mass are listed in Table 1.

**Table 1.** Basic properties for rock layers.

| Lithology | Young's Modulus (GPa) | Poisson's Ratio | Density (kg/m$^3$) | Porosity | Permeability (m$^2$) | Biot-Willis Coefficient |
|---|---|---|---|---|---|---|
| Carbonate | 55 | 0.26 | 2700 | 0.18 | $1 \times 10^{-13}$ | 0.8 |
| Salt | 25 | 0.3 | 2200 | 0.005 | $1 \times 10^{-20}$ | 0.1 |

Initial temperature is defined using a basin-scale geothermal gradient derived from bottom-hole temperature regressions in the Michigan Basin. Shahmohammadi and Maghoul report a present-day gradient of approximately 19.2 °C/km, described by

$$T(°C) = 14.5 + 0.0192z \quad (23)$$

where z is depth in meters [35]. Applying this relation to depths of 0.9–1.06 km yields initial temperatures of 32 °C at the top of the B salt and 35 °C at the base of the A-2 salt. Although this geothermal gradient is moderate and no high-enthalpy geothermal resource is targeted, temperature still influences $CO_2$ density, viscosity and compressibility, as well as thermoelastic stress changes in the surrounding rock during cyclic injection and production.

Non-isothermal effects are therefore retained in the model to capture the thermal buffering role of the formation and the feedback of temperature on pressure and stress evolution. The injected $CO_2$ is assigned a constant temperature of 32 °C, slightly lower than the undisturbed reservoir temperature but above the critical temperature of $CO_2$ (31.1 °C). This choice minimizes thermal shock to the rock mass, maintains supercritical conditions at the simulated reservoir pressures, and allows the formation heat to act primarily as a thermal buffer that gradually warms the injected $CO_2$ during cyclic operation rather than as a separate geothermal energy source. The detailed thermal properties of the rock mass and brine are listed in Table 2.

**Table 2.** Thermal properties for rock layers.

| Lithology | Heat Capacity (J/(kg·K)) | Thermal Conductivity (W/(m·K)) | Coefficient of Thermal Expansion (1/K) |
|---|---|---|---|
| Carbonate | 850 | 3.5 | $9 \times 10^{-6}$ |
| Salt | 850 | 6.0 | $3.75 \times 10^{-5}$ |

Initial pore pressure is assumed hydrostatic with respect to formation brine, taking the Lake Huron water surface as the reference head. At 900 m below the lake, the hydrostatic pore pressure is approximately 9 MPa, increasing to 10.4 MPa at 1060 m depth. This is consistent with regional hydrogeologic modeling and site investigations indicating that deep Paleozoic formations in southwestern Ontario, including the Silurian Salina units, form a low-permeability, saline groundwater system with pressures close to hydrostatic or slightly underpressured rather than strongly overpressured [36]. Initially, the reservoir was assumed to be fully saturated with brine. To avoid numerical singularity, a small initial $CO_2$ saturation of 0.05 was imposed throughout the domain.

Prior to cyclic operation, a cushion-gas injection stage is simulated in order to displace brine away from the near-wellbore region and establish a $CO_2$-filled pore space within the A-2 carbonate. This pre-filling step is necessary to create a stable supercritical $CO_2$ working volume, reduce early-time brine production, and decouple the subsequent cyclic response from the arbitrary initial brine distribution. It also mimics standard practice in underground gas storage, where a permanent cushion volume is maintained to stabilize reservoir pressure, improve injectivity and deliverability, and provide a consistent thermodynamic operating window for repeated charge-discharge cycles. In this pre-filling phase, supercritical $CO_2$ is injected at a constant mass flow rate of 8 kg/s, starting from an initially brine-saturated reservoir. Buoyancy-driven segregation causes the injected $CO_2$ to accumulate preferentially toward the upper part of the reservoir interval, forming a laterally continuous $CO_2$-rich zone beneath the B salt while more residual brine remains in the lower part of the A-2 carbonate.

On this cushion-gas background, three cyclic operating strategies are examined to evaluate the impact of well completion and production allocation on storage performance. Each case was first simulated for two years under the prescribed 24 h injection-production cycle. The final pressure, saturation, temperature, and displacement fields from this two-year cyclic simulation were then used directly as the initial state for an additional five-month simulation with a refined time step, with no conditions changed in this stage. This refined window was used to resolve intra-cycle variations and short-term cycle-to-cycle trends in greater detail. In the base case, the entire perforated interval of the A-2 carbonate is used for both injection and production, with 6 kg/s of $CO_2$ injected for 12 h followed by production at the same rate for 12 h, representing a symmetric 24 month charge-discharge cycle. In the second scenario, only the upper half of the perforated interval is opened during production

while injection still occurs over the full reservoir thickness; production is retained at 6 kg/s through the upper half of the well to explore the effect of targeting the $CO_2$-enriched zone while keeping the total daily mass balance comparable to the base case. In the third scenario, production is vertically distributed, with 4 kg/s produced from the upper half of the completion and 2 kg/s from the lower half, again focusing on how preferentially drawing from the $CO_2$-rich upper interval versus the brine-richer lower interval influences pressure evolution, $CO_2$ recovery and the thermal-hydraulic response of the A-2 carbonate.

The numerical domain was discretized using a non-uniform tetrahedral mesh to balance computational efficiency and accuracy. Local mesh refinement was applied around the vertical well, where strong gradients of pressure, temperature and Darcy velocity are expected during cyclic injection-production. Within a 5 m radius around the well, a swept hexahedral mesh was employed to better resolve the near-wellbore flow and gradient structure and to improve numerical stability. The minimum element size in the vicinity of the well trajectory was set to 0.8 m, gradually increasing to 20–30 m toward the lateral boundaries to limit the total element count while maintaining adequate resolution in the near-wellbore region and across material contrasts. This configuration allows accurate representation of the A-2 carbonate reservoir, the overlying and underlying halite caprocks, and the steep pressure and saturation gradients that develop around the completion interval. To ensure numerical reliability, a mesh-independence check was performed by comparing reservoir pressure and temperature fields under identical cyclic loading conditions for a medium and a refined mesh. Differences in key response metrics were found to be within 1–2%, confirming that the adopted mesh resolution is sufficient to capture the coupled thermo-hydraulic-mechanical behavior of the system. Although a full multi-level refinement study was not carried out due to computational cost, the observed convergence indicates that the chosen mesh provides a robust compromise between accuracy and efficiency for the simulation.

This work provides an initial step toward evaluating the feasibility of compressed $CO_2$ energy storage in the Salina B–A-2 system beneath offshore Lake Huron, but several simplifications must be acknowledged. The stratigraphic model is treated as laterally uniform and horizontally layered, without explicitly representing facies transitions, small-scale heterogeneities or faults, any of which could locally modify pressure propagation and flow pathways. $CO_2$ leakage into the overlying and underlying halite caprocks is neglected based on their very low intrinsic permeability, so that potential loss through fractures or disturbed zones around wells is not captured. Geochemical reactions are only implicitly considered through an optimistic choice of reservoir permeability rather than reactive transport, and wellbore hydraulics and thermal losses are not modelled explicitly. These assumptions tend to favour efficient pressure communication and $CO_2$ recovery and may therefore produce optimistic estimates of storage performance and operational stability. Future work should incorporate site-specific heterogeneity, explicit two-phase flow and reactive processes, and more detailed well and caprock representations to provide a more comprehensive and conservative assessment of CCES behavior in the Salina Group under realistic subsurface conditions.

## 5. Modeling Results

### *5.1. Cushion-Gas Injection*

During the pre-filling stage, supercritical $CO_2$ is injected at a constant rate of 8 kg/s into the initially brine-saturated A-2 carbonate. Figure 2a–c demonstrate 3D $CO_2$ saturation of the reservoir after 1, 5 and 8 months of injection, respectively, while Figure 3a–c present vertical slices through the reservoir at the same times. After about 1 month, a compact $CO_2$ plume has formed around the well, with a maximum saturation of 0.56 confined to a

limited radial extent. The plume is already strongly asymmetric in the vertical direction. $CO_2$ occupies mainly the upper part of the A-2 carbonate directly beneath the B salt, whereas the lower part of the reservoir remains brine-dominated. This observed plume geometry is controlled by the interaction of buoyancy and the limited reservoir thickness. Because supercritical $CO_2$ is less dense than brine, the plume rapidly traverses the 40 m vertical reservoir section and impinges on the impermeable B-salt top, after which further upward motion is arrested and the injected $CO_2$ is preferentially redistributed as a laterally spreading in the caprock-parallel layer.

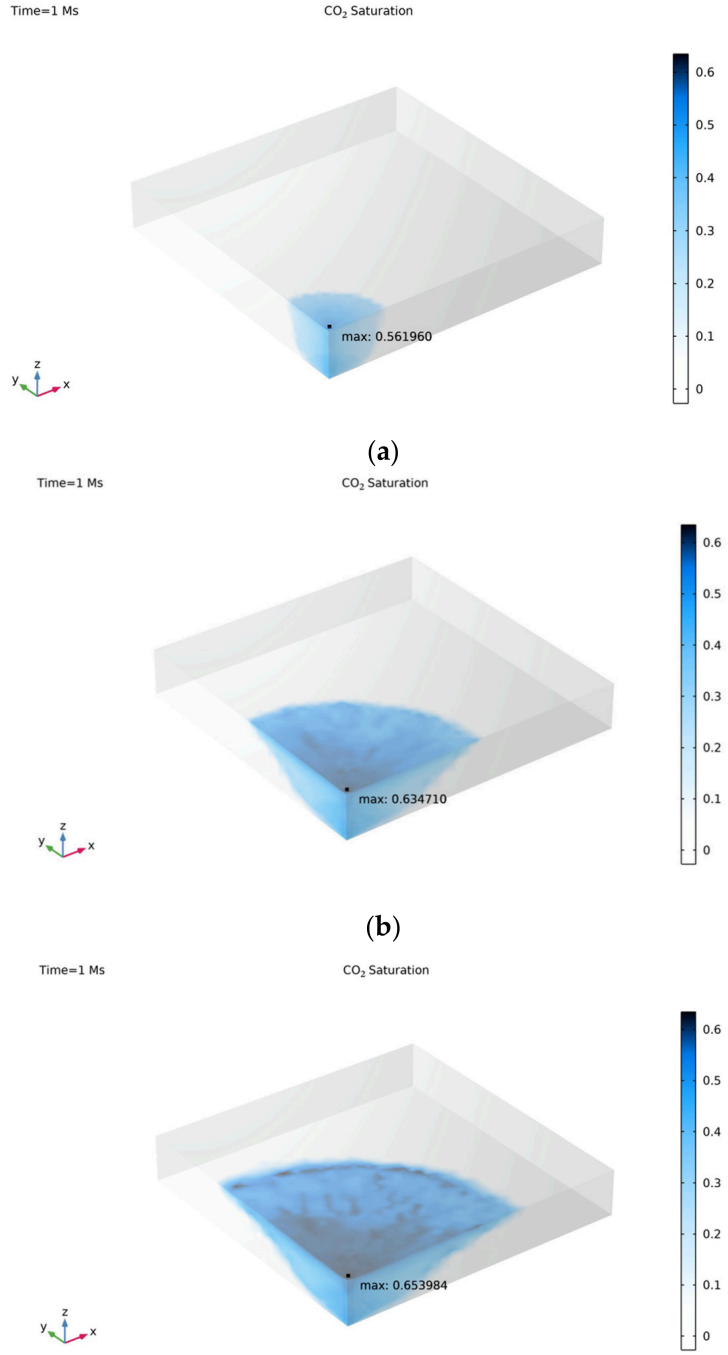


**Figure 2.** $CO_2$ saturation of the reservoir after (**a**) 1 month, (**b**) 5 months, (**c**) 8 months of simulation.

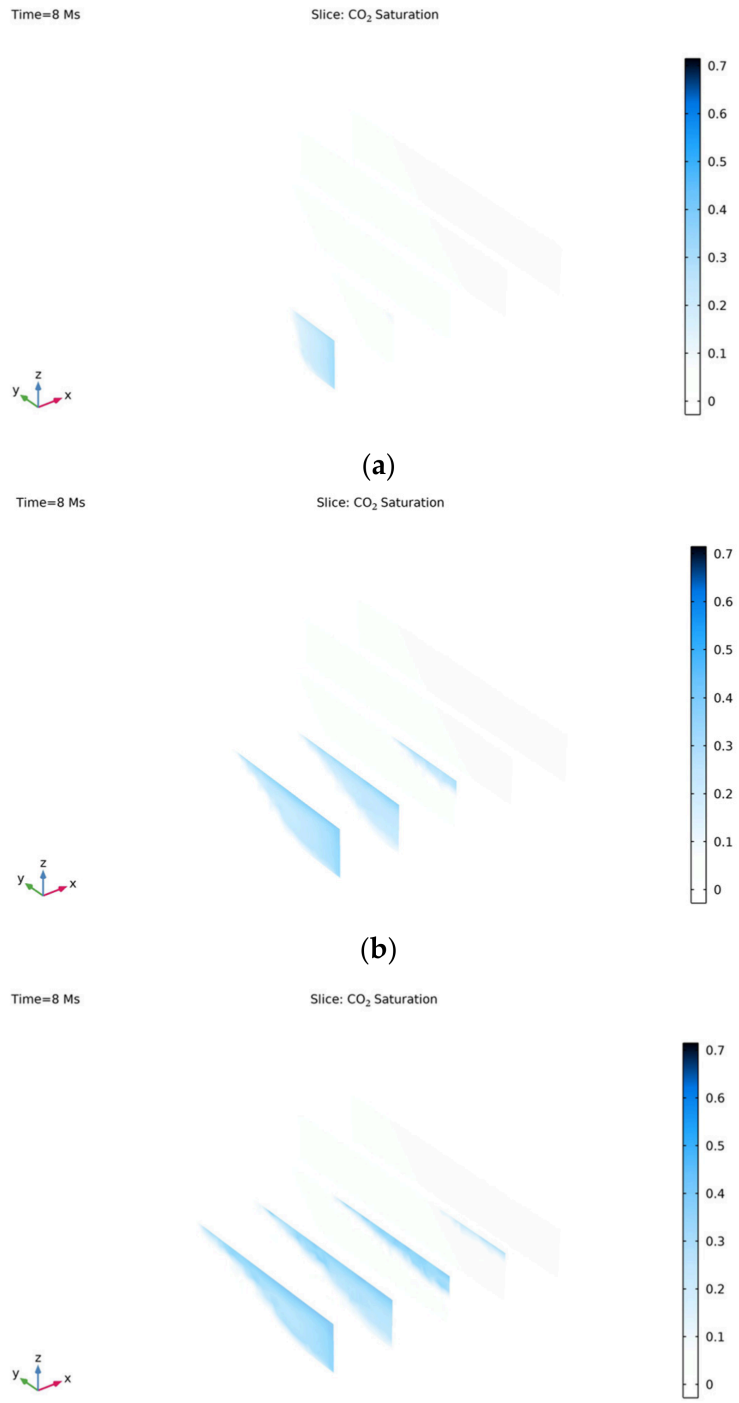


**Figure 3.** Vertical slices of $CO_2$ saturation through the reservoir after (**a**) 1 month, (**b**) 5 months, (**c**) 8 months of simulation. These cross-sectional views complement the corresponding 3D saturation distributions shown in Figure 2 and highlight the vertical segregation and caprock-parallel spreading of $CO_2$ beneath the upper salt layer.

By 5 months of injection, the $CO_2$ front has migrated laterally along the reservoir top to a radial distance of roughly 250 m from the well. The plume geometry evolves into a broad wedge beneath the B salt, with $CO_2$ saturation in the uppermost part of the reservoir reaching 0.63 around well and gradually tapering downward toward the reservoir mid-depth. In contrast, the lower few metres of the A-2 carbonate retain only modest

$CO_2$ saturation, and both the extent of the lower gas-filled zone and saturation show little growth compared with the 1-month results. This indicates that, once a continuous $CO_2$ layer has formed beneath the B-salt caprock, plume evolution becomes strongly buoyancy-dominated: $CO_2$ injected into the lower part of the completion is rapidly redistributed upward, and a quasi-steady balance is reached between local injection near the well and upward migration toward the reservoir top. Consequently, the lower portion of the reservoir remains largely brine-filled with a nearly stable, thin gas interval, while most incremental injected mass contributes to the lateral expansion and thickening of the caprock-parallel $CO_2$ wedge in the upper reservoir. This behavior is further illustrated by vertical slices of saturation. In the slice intersecting the well, $CO_2$ saturation reaches 0.62 and occupies almost the full upper part of the A-2 carbonate, whereas slices 100–200 m away show progressively thinner wedges with lower peak saturation. This systematic thinning and attenuation of the $CO_2$ layer with distance from the well confirms a transition from advection-dominated filling in the near-well region to a more diffuse, buoyancy-assisted migration front in the far field. This distribution provides a favorable initial condition for subsequent cyclic operation, combining a high-saturation $CO_2$ zone in the near-well region with a relatively stable brine column at the base of the reservoir that helps damp pressure fluctuations and limits early-time brine production.

After 8 months, the $CO_2$ plume continues to spread radially beneath the reservoir top. The high-saturation wedge occupies much of the inner model domain, and the maximum saturation near the well increases slightly to about 0.65. Vertical slices through the A-2 carbonate reveal that the gas distribution is no longer simply centered on the well: in the slice intersecting the well, $CO_2$ forms a relatively uniform caprock-parallel lens with peak saturation at 0.62, whereas in the adjacent slice that passes beyond the well, the highest saturation is located near the plume front. Farther out, slices show a progressively thinner layer with reduced maxima. This pattern indicates that, once a continuous $CO_2$ layer has developed beneath the B-salt caprock, ongoing injection drives lateral accumulation of $CO_2$ toward the advancing front, while advection near the well and buoyancy-assisted spreading in the far field jointly produce a smooth transition from $CO_2$-rich to brine-dominated regions around the well. At this stage, plume growth is increasingly controlled by diffusion and dispersion, and $CO_2$ accumulating at the far leading edge is unlikely to be effectively recovered during subsequent cyclic operation; from a CCES perspective, further extension of the cushion-gas injection period therefore provides little additional benefit. The increase in peak $CO_2$ saturation becomes limited after the first several months, rising from about 0.56 after 1 month to 0.63 after 5 months and only slightly further to about 0.65 after 8 months. This suggests that the cushion-gas stage becomes progressively less efficient at increasing near-well working saturation; continued injection mainly expands the distal caprock-parallel plume rather than substantially increasing the recoverable high-saturation zone around the well.

The associated pore pressure field after 5 months of injection (Figure 4) exhibits a nearly radial pressure distribution centred on the well, with reservoir pressures ranging from about 10.6 MPa in the far field to 11.9 MPa at the wellbore. Relative to the initial hydrostatic pressure of approximately 9–10.4 MPa across the model depth interval, this pressure increase remains moderate and localized. This indicates that the selected cushion-gas injection rate is sufficient to establish a $CO_2$ working volume without producing a large basin-scale overpressure response, and that the B and A-2 salt caprocks experience only limited additional hydraulic loading during the cushion-gas stage. The first principal stress field (Figure 5) retains the initial depth-dependent layering imposed by the overburden, while showing a localised perturbation around the well where increased pore pressure slightly reduces the magnitude of compressive principal stress in the A-2 carbonate.

Importantly, no large stress reversals or concentrations develop in the caprock, indicating that the chosen injection rate keeps the system within a mechanically stable regime during pre-filling.

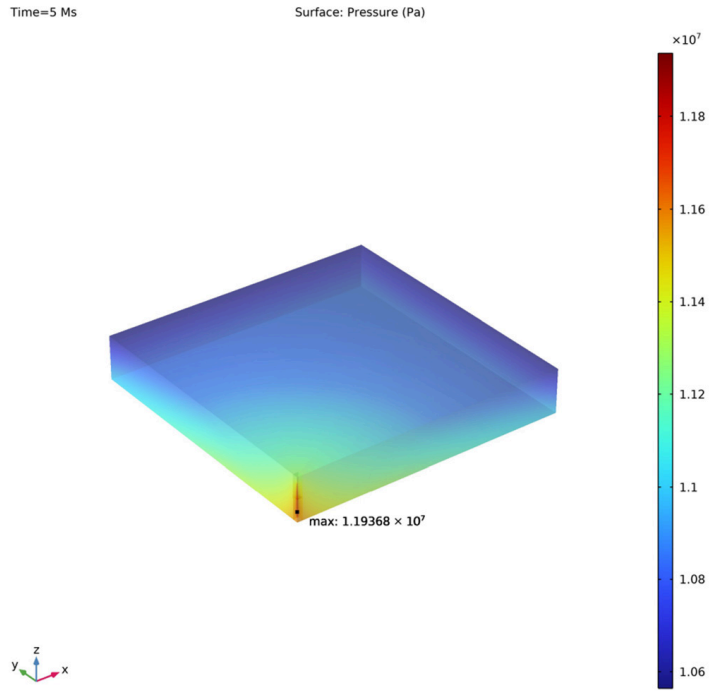


**Figure 4.** Pore pressure field after 5 months.

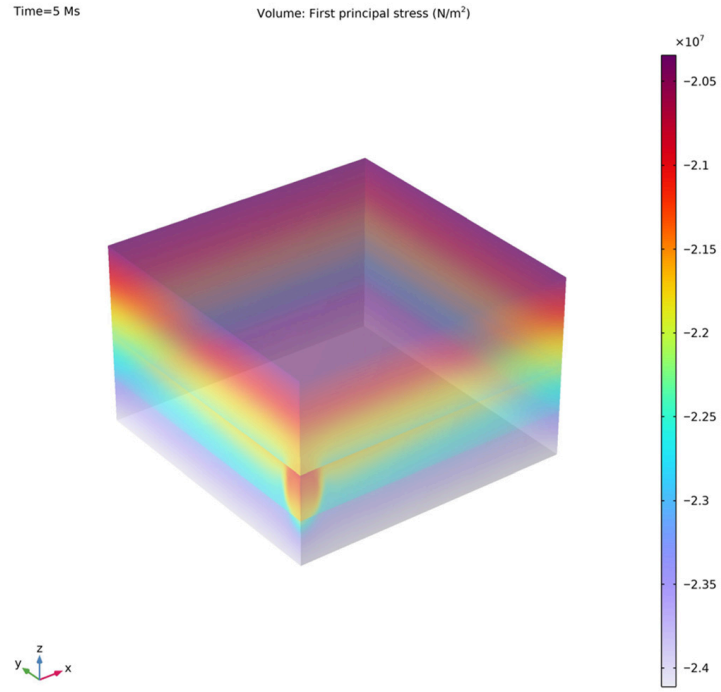


**Figure 5.** First principal stress field after 5 months.

Finally, the temperature evolution remains minor during the cushion-gas injection (Figure 6). The injected $CO_2$ at 32 °C (305 K) is only slightly cooler than the undisturbed reservoir (≈33–35 °C), so the resulting thermal perturbation is limited to about 1–2 K near the well and upper reservoir, with the background geothermal gradient largely preserved throughout the domain. These results confirm that the pre-filling stage mainly establishes

a pressure-controlled $CO_2$ cushion, with only minor thermal disturbance. This is consistent with the model assumption that formation heat acts as a stabilising thermal buffer rather than a primary energy source.

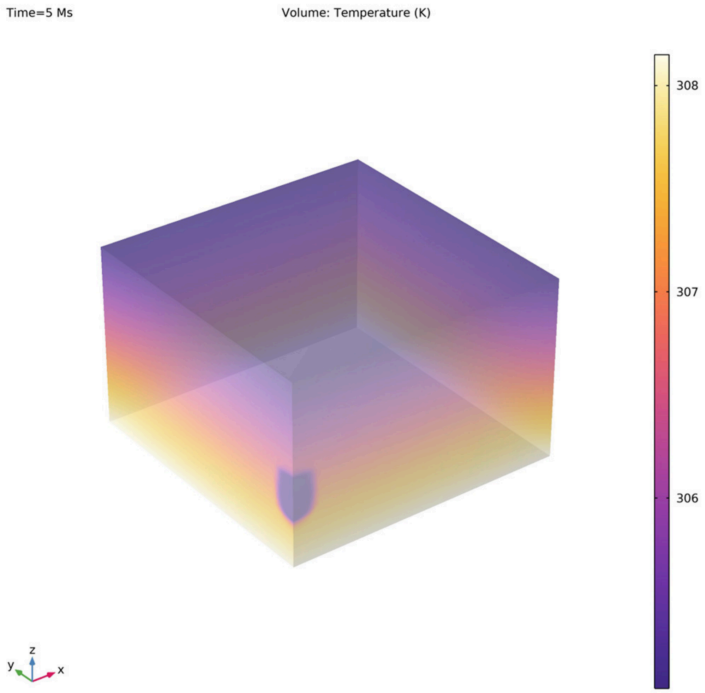


**Figure 6.** Temperature field after 5 months.

### *5.2. Cyclic Injection-Production Performance*

After 5 months of cushion gas injection, the A-2 carbonate contains a laterally continuous $CO_2$ wedge pinned to the upper caprock, with peak saturation of about 0.6–0.7 near the well and a brine-dominated lower interval. On this basis, 24 h cycles of injection and production are imposed and simulated for two years, followed by an additional five-month period resolved at high temporal resolution. Three completion strategies are examined: a full-length case in which the entire perforated interval is produced, a case where production is restricted to the upper half of the well, and a split-completion configuration in which the upper and lower halves are produced at different rates. Figures 7–9 show $CO_2$ saturation maps at the end of injection and production for 0, 2.5 and 5 months. Across all three schemes, the large-scale plume geometry established during cushion injection is largely preserved. Injection rebuilds a high-saturation zone around the well and reconnects it with the caprock-parallel wedge, whereas production creates only a local depletion zone without disrupting the upper gas layer. With increasing cycle number, saturation continues to be strongly vertically structured. In the lower part of the A-2 carbonate, $CO_2$ saturation shows a slight decrease during the early cycles as gas is redistributed upward; this downward depletion trend weakens over time as a quasi-steady state is approached. In the mid-reservoir, saturation continues to decline over the refined window, whereas in the upper 10–15 m beneath the B-salt caprock a gradual increase in saturation persists. This pattern suggests slow upward migration of $CO_2$ from the lower reservoir into the upper gas wedge. As buoyancy-driven segregation and production-driven depletion approach equilibrium, cyclic operation mainly redistributes $CO_2$ within the existing wedge rather than mobilising substantial additional gas from depth.

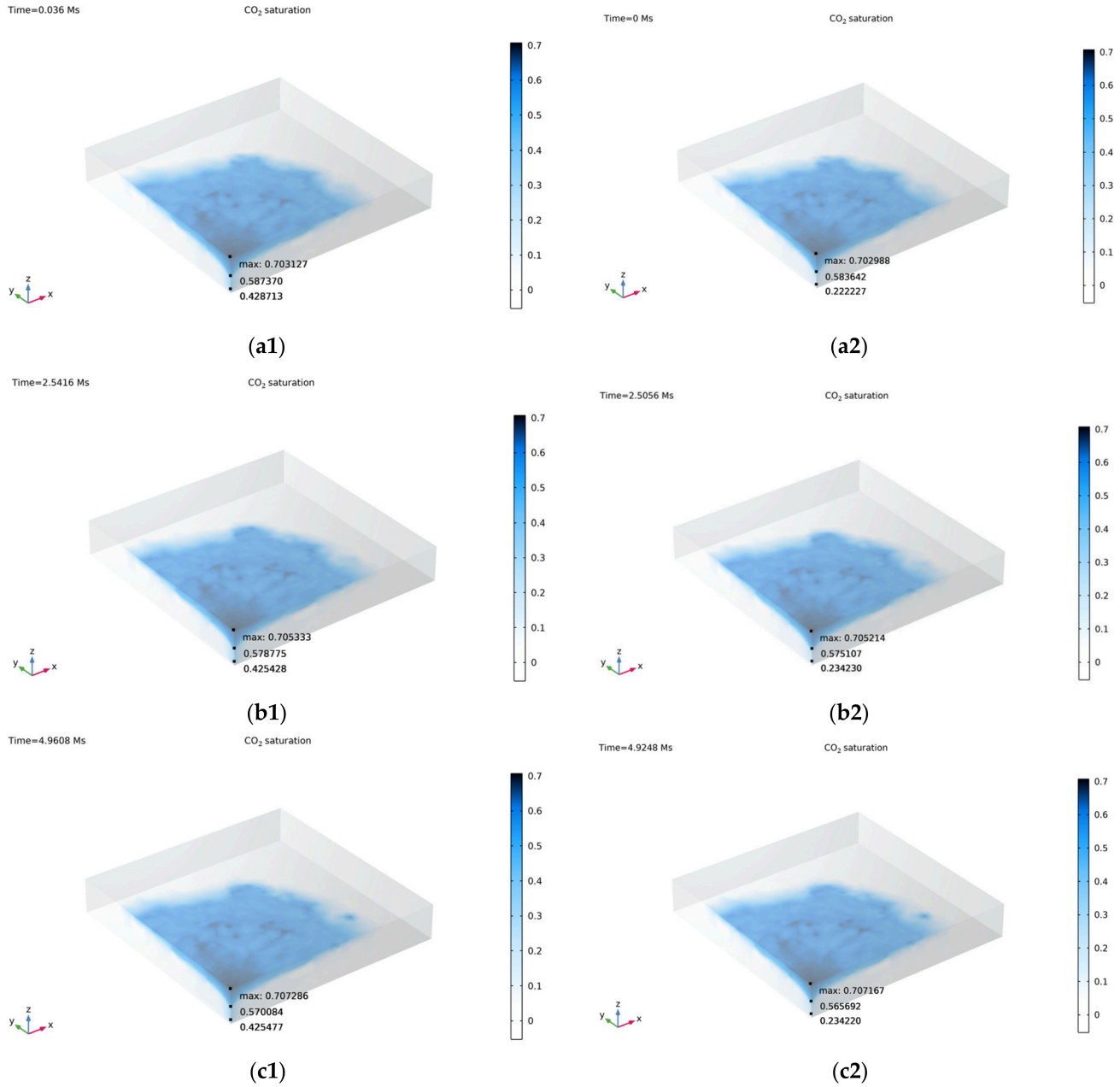


**Figure 7.** $CO_2$ saturation distribution of the full-length completion case after 12 months of injection-production cycling followed by 5 months of refined cyclic simulation. Panels (**a1**,**a2**), (**b1**,**b2**), (**c1**,**c2**) correspond to 0, 2.5 and 5 months after the start of cyclic operation, respectively. For each pair of panels, the left plot shows the saturation field at the end of an injection half-cycle, and the right plot shows the corresponding field at the end of the subsequent production half-cycle.

The three completion strategies have only a minor influence on the large-scale plume geometry, but they lead to discernible differences in how the near-well region is mobilised. In the full-length case, production taps both the upper gas-rich band and the lower brine-buffer zone, yielding a relatively broad but diffuse low-saturation region around the well after each production phase, while the end-of-injection maps show the widest lateral extent of the caprock-parallel $CO_2$ wedge for a given cycle, reflecting the fact that the entire 40 m interval participates to some degree in recharge. At the same time, the lower $CO_2$ wedge exhibits the lowest average saturation and the narrowest zone of $CO_2$ enrichment among the three completion strategies, indicating that any further increase in net withdrawal would primarily drain this already gas-poor interval and weaken its ability to sustain

upward replenishment of the caprock-proximal gas layer, potentially hindering upward replenishment and, over longer timescales, reducing the effective $CO_2$ fraction in the produced fluid. The upper-only completion, by contrast, concentrates flow within the caprock-proximal wedge. At the end of injection, saturation maps show the highest peak $CO_2$ saturations near the well but also the smallest laterally swept area. At the end of production, only a narrow depletion zone develops around the wellbore, while the surrounding gas cap remains comparatively compact. In this configuration the produced fluid is strongly $CO_2$-rich, the actively swept gas volume is the smallest of the three cases, and the lower reservoir remains largely unchanged during cyclic operation. The slight decrease in $CO_2$ saturation at lower reservoir over successive cycles indicates a slow, buoyancy-driven leakage of gas from the lower interval into the upper wedge, where it is produced, so that the lower reservoir evolves into a quasi-steady pressure buffer and a weak long-term $CO_2$ source feeding the caprock-proximal gas layer. The split-completion case shows an intermediate response. Moderate mobilisation of the lower interval increases the vertically affected zone and slightly reduces peak $CO_2$ saturation near the caprock relative to the upper-only case. Laterally, the plume extends farther than in the upper-only case but remains less extensive than in the full-length case; the production-related depletion footprint is also intermediate. As a result, both the lateral extent of the $CO_2$-rich region and the characteristic saturation levels at the end of injection and production fall between those obtained for the full-length and upper-only configurations, confirming that completion strategy mainly redistributes where within the 40 m interval gas is cycled, rather than fundamentally altering the overall plume architecture.

Across the three completion schemes the $CO_2$ production rate per cycle remains very stable, but with clear systematic differences in level and trend. For the full-length completion, the production curve is weakly non-monotonic. During roughly the first ten cycles the average $CO_2$ rate increases slightly, because the near-well interval is still transitioning from a brine-dominated state to a $CO_2$-dominated one. As cycles proceed, more of the 40 m perforated section is swept by $CO_2$, brine is flushed out, and gas saturation and gas relative permeability around the well both increase; therefore, a slightly higher $CO_2$ mass flow is delivered. Once a stable gas wedge has formed along the upper part of the reservoir and the lower interval has adjusted to its role as a brine buffer, this charging phase ends. From that point onward the system behaves like a mature storage reservoir: small cumulative losses of $CO_2$ from the swept region like buoyant leakage into the far field and residual trapping during each cycle gradually reduce the local gas saturation and mobility, so the per-cycle $CO_2$ rate begins a very gentle decline of only 360 kg/cycle over the remaining cycles. It should be noted that this initial non-monotonic segment of the full-length curve is partly a start-up transient associated with using the 2-year simulation result as the initial condition rather than a fully periodic steady state. At the end of this long stage, pressure and saturation around the well are still evolving; when additional cyclic injection-production is imposed, the near-well region needs several cycles to re-equilibrate to the new boundary conditions. Although this initial increase in $CO_2$ production is partly a numerical start-up transient associated with switching from the preceding long-term operation to cyclic operation in a new study, the underlying physics is analogous to field situations where a reservoir is shut in or operated under quasi-static conditions and then brought into another cycling. This short start-up adjustment is confined to the first few cycles and does not materially affect the subsequent quasi-steady production behavior or the long-term performance assessment.

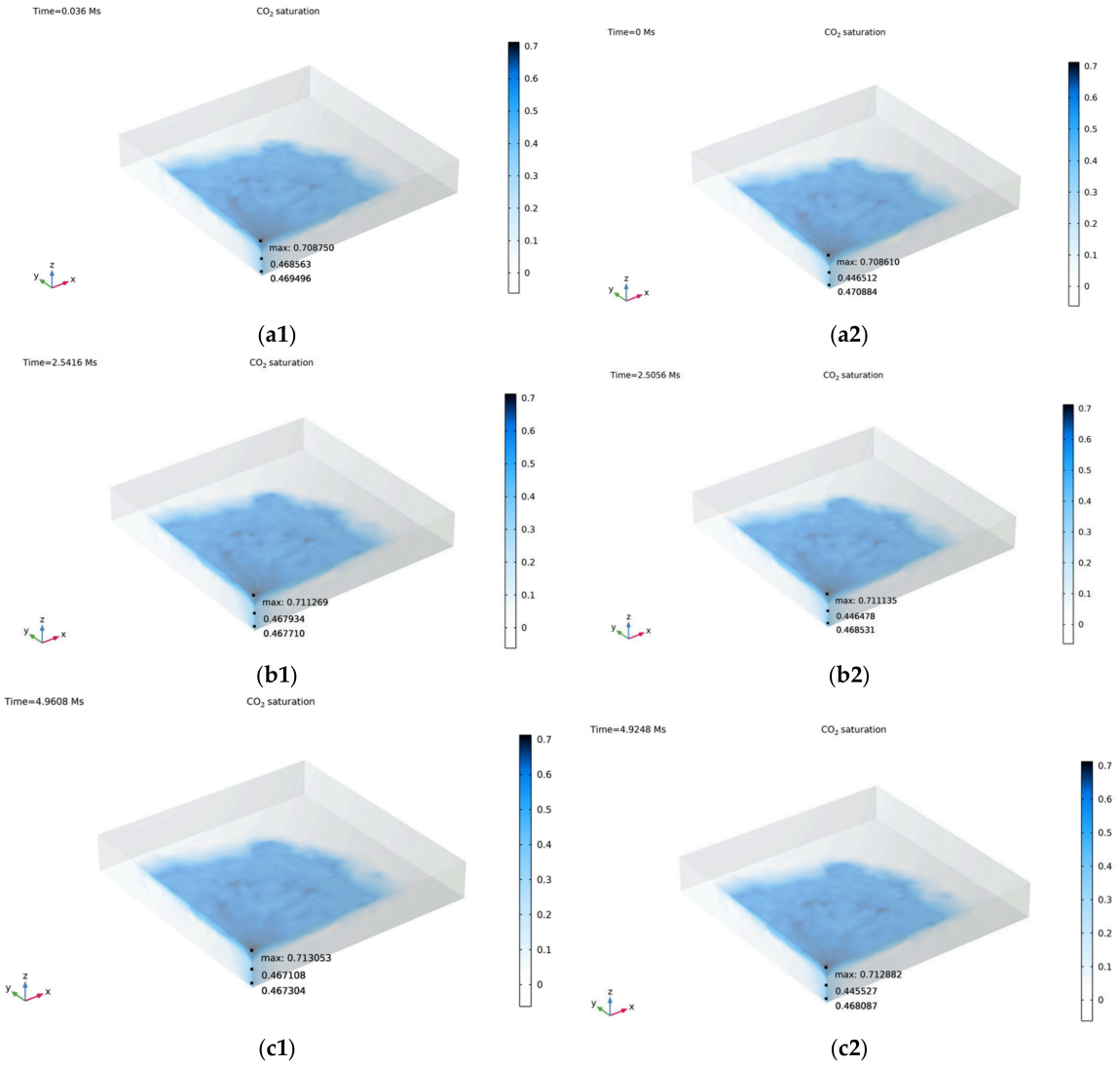


**Figure 8.** $CO_2$ saturation distribution of the half-length completion case after 12 months of injection-production cycles followed by 5 months of refined cyclic simulations. Panels (**a1**,**a2**), (**b1**,**b2**), (**c1**,**c2**) correspond to 0, 2.5 and 5 months after the start of cyclic operation, respectively. For each pair of panels, the left plot shows the saturation field at the end of an injection half-cycle, and the right plot shows the corresponding field at the end of the subsequent production half-cycle.

For the upper-only completion, the average $CO_2$ production rate is the highest (~213,120 kg/cycle at the beginning of the refined window) and is dominated by flow from the caprock-proximal gas cap. Because the actively swept volume is confined to the upper half of the reservoir, the time series shows an almost strictly monotonic decline, with the mean rate dropping by about 576 kg/cycle over all cycles. A very small irregularity appears over the first few cycles, but it is much less pronounced than in the full-length case, because the cyclic boundary conditions act directly on the already gas-rich upper interval and require only limited readjustment of near-well saturation and relative permeability. Once this brief adjustment is completed, the curve follows a smooth, gentle downward trend. The decline remains modest but is relatively steeper than for the full-length completion, consistent with gradual depletion of a smaller effective working volume that is cycled more intensively from one day to the next. Operationally, the smooth and nearly monotonic response suggests that the upper-only configuration is less sensitive to small operating perturbations and provides more predictable $CO_2$ output during the simulated period.

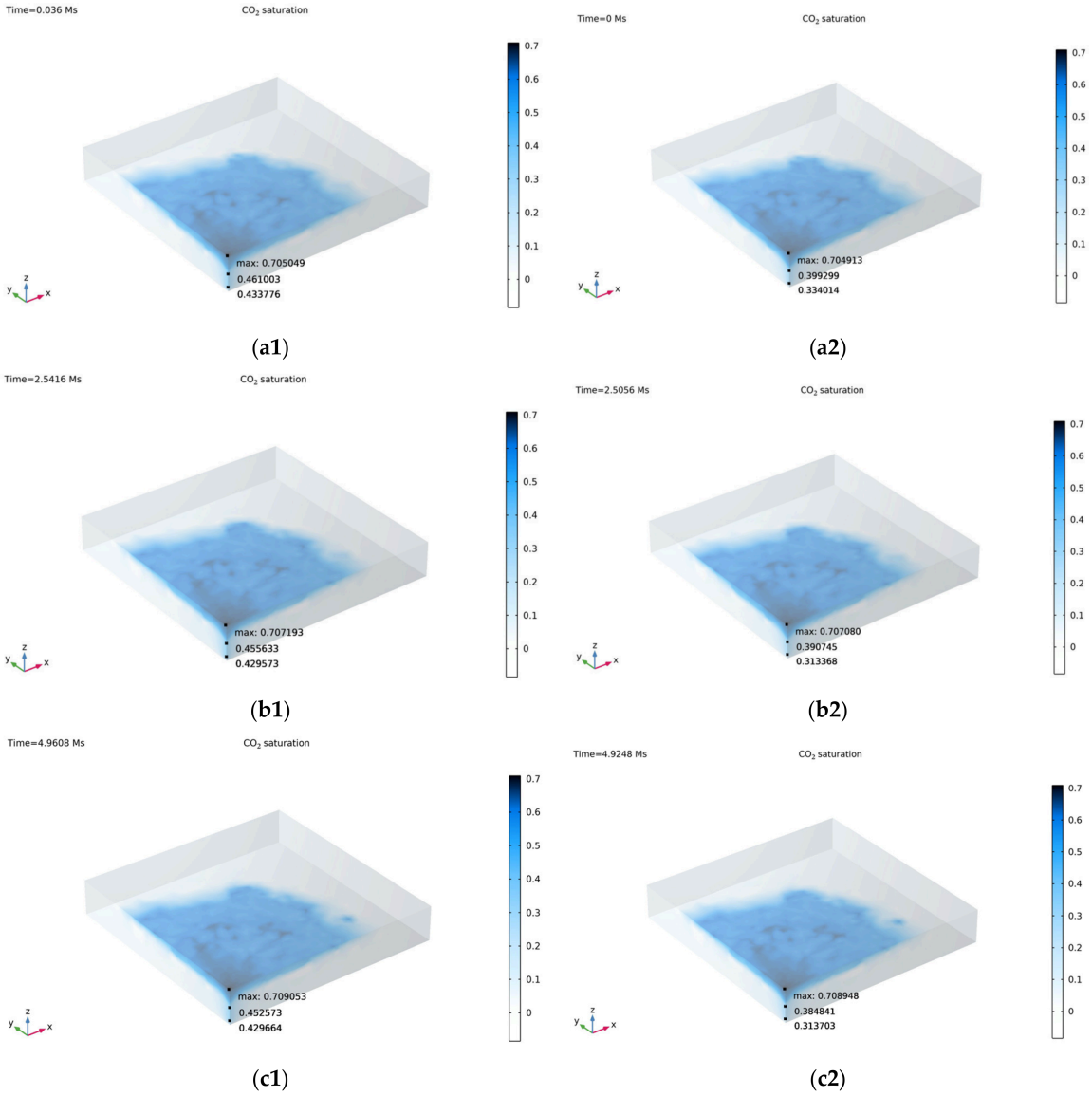


**Figure 9.** $CO_2$ saturation distribution of the split-length completion case after 12 months of injection-production cycles followed by 5 months of refined cyclic simulations. Panels (**a1**,**a2**), (**b1**,**b2**), (**c1**,**c2**) correspond to 0, 2.5 and 5 months after the start of cyclic operation, respectively. For each pair of panels, the left plot shows the saturation field at the end of an injection half-cycle, and the right plot shows the corresponding field at the end of the subsequent production half-cycle.

For the split-completion case, the behavior falls between the two end-members in both absolute rate and temporal trend. The initial average $CO_2$ production rate (~210,960 kg/cycle at the start of the refined window) is slightly lower than in the upper-only configuration but clearly higher than for the full-length completion. Over the simulated cycles the curve decreases monotonically by about 648 kg/cycle, reflecting that part of the flow is drawn from the lower, more brine-rich interval as well as from the caprock-proximal gas cap. As cycling proceeds, gradual replacement of $CO_2$ by brine in the lower perforations and mild depletion of the upper wedge both contribute to the observed decline. The few minor wiggles at early times are small compared with the overall trend and indicate only a short adjustment as the coupled upper-lower flow pattern establishes itself; thereafter, the rate evolution is smooth and nearly linear. In relative terms, the decline rate sits between the upper-only and full-length schemes, consistent with a working volume and degree of brine involvement that are also intermediate between those two configurations.

Despite these differences, the production decline is small relative to the total mass produced per cycle (Figure 10). Across the refined window, the change remains below 1%, indicating that all three strategies maintain stable working-gas output over the analysed period. The main distinction among the cases is therefore not a loss of overall deliverability, but the vertical distribution of the active working volume and the degree to which the lower brine-rich interval participates in production.

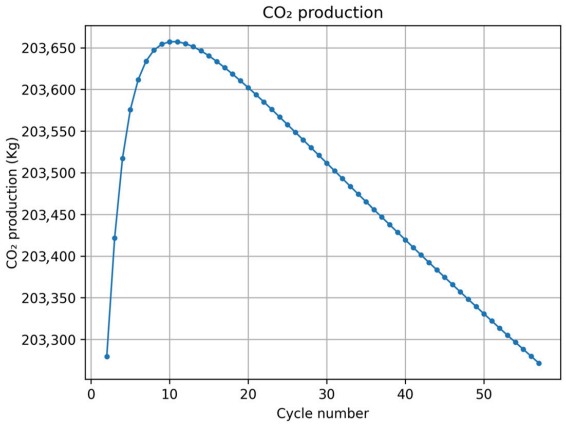


(**a**)

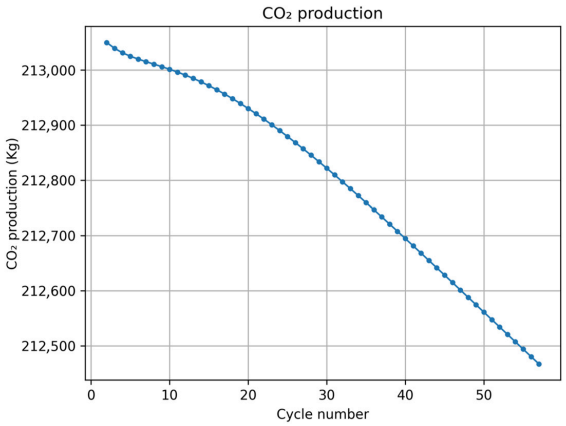


(**b**)

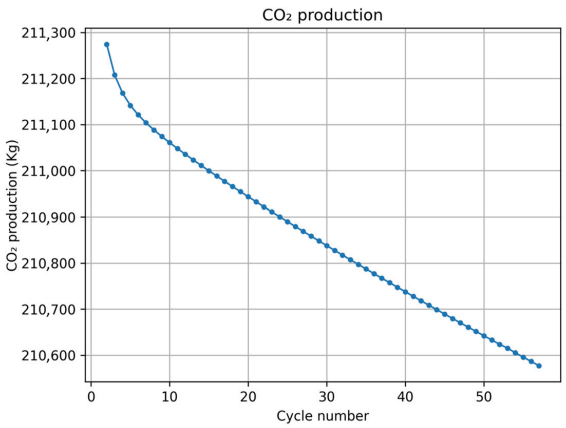


(**c**)

**Figure 10.** Evolution of average $CO_2$ production rate per cycle for the three completion strategies. Figures (**a**), (**b**), (**c**) correspond to full-length completion, half-length completion, split-length completion after the start of cyclic operation, respectively.

Pore-pressure maps after additional five months of cyclic operation show that the pressure disturbance remains strongly localized around the well and only weakly dependent on the completion strategy (Figure 11). In all cases, the reservoir pressure field is close to

the initial hydrostatic profile (~9–10 MPa) away from the well, while a narrow overpressured cone develops during injection and a corresponding underpressured cone forms during production.

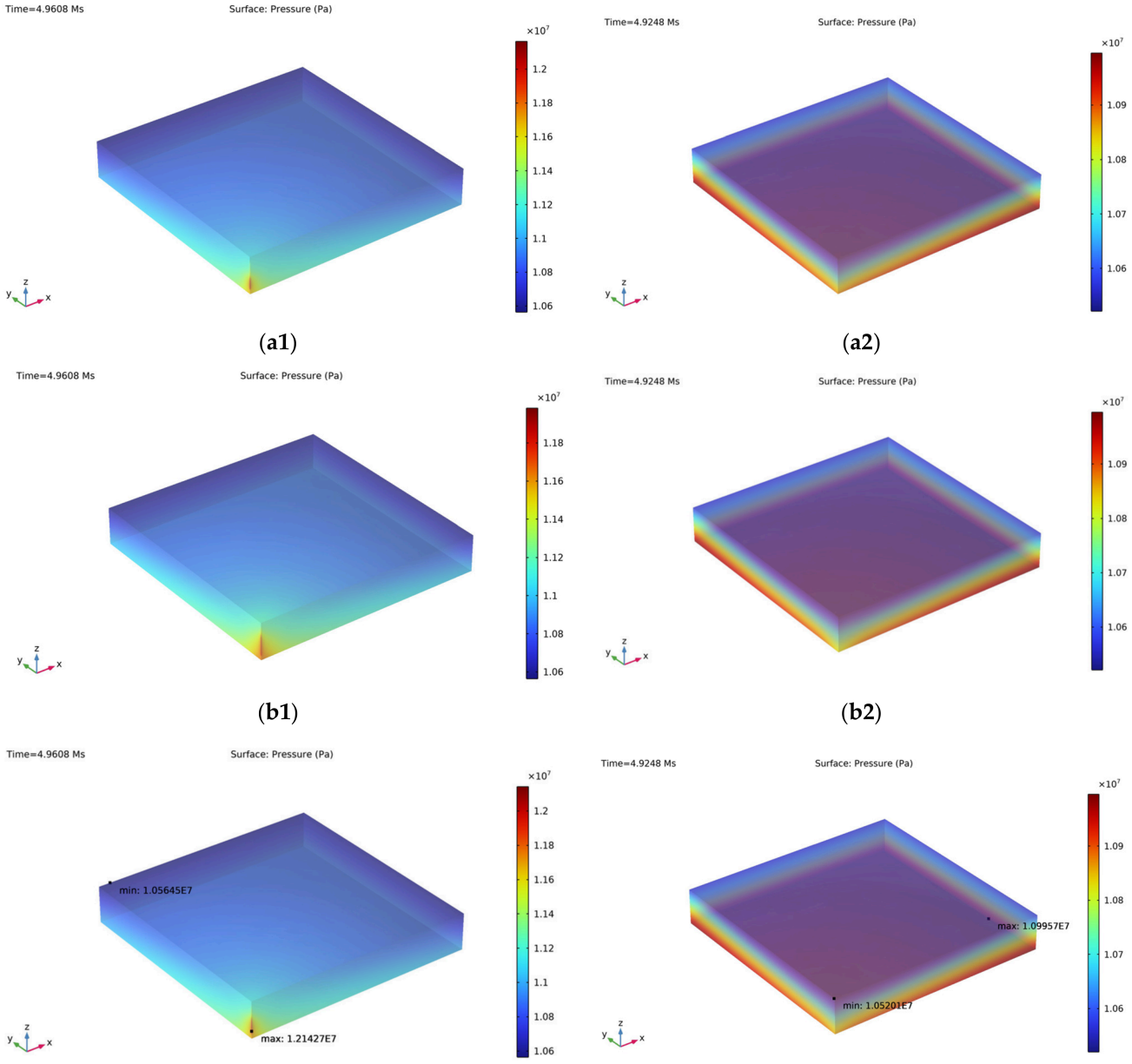


**Figure 11.** Pore pressure distribution after 12 months of injection-production cycles followed by 5 months of refined cyclic simulations. Panels (**a1**,**a2**), (**b1**,**b2**), (**c1**,**c2**) correspond to full-length completion, half-length completion, split-length completion after the start of cyclic operation, respectively. For each pair of panels, the left plot shows the pore pressure field at the end of an injection half-cycle, and the right plot shows the corresponding field at the end of the subsequent production half-cycle.

For the full-length completion, end-of-injection results display a nearly symmetric pressure build-up along the 40 m perforated interval: the overpressure maximum is centred at the well, and the vertical pressure gradient within the A-2 carbonate is modest, because injection is distributed over the entire thickness. After production, a broad but relatively diffuse drawdown zone appears around the wellbore; pressure recovers rapidly with distance so that beyond a few hundred metres the reservoir remains essentially hydrostatic.

This behavior is consistent with the saturation maps, where both the upper gas-rich band and the lower brine-rich interval participate in the flow and share the pressure perturbation.

In the upper-only completion, the injection phase is identical in terms of total mass rate, so the end-of-injection pressure cone is very similar in amplitude to the full-length case but more clearly skewed toward the upper part of the reservoir. Because production is confined to the upper perforations, the end-of-production maps show a stronger and more compact drawdown immediately beneath the B-salt, while the lower half of the A-2 carbonate experiences only a small pressure change. This pattern matches the saturation results, where the upper gas cap is actively swept while the lower zone acts largely as a pressure buffer. In practice this implies that cyclic loading is concentrated near the caprock, whereas the deeper part of the reservoir shields the system from large far-field pressure swings.

The split-completion configuration produces an intermediate response. During injection, the pressure build-up is again similar in magnitude but slightly more vertically uniform than in the upper-only case, reflecting that flow is allowed along the full interval. At the end of production, drawdown is distributed over both upper and lower perforations: the minimum pressures near the well are somewhat higher than in the upper-only case because the same total production is spread over a larger cross-section, and the under-pressured volume extends a little deeper than in the full-length completion. This agrees with the $CO_2$ saturation patterns, where a thicker interval is mobilised but the plume remains top-skewed.

Figure 12 shows the evolution of average pressure along the perforated well interval over the additional five months of cyclic operation for the three completion schemes. In all three cases, the segment-averaged pressure along the perforated interval follows a clear 24 h saw-tooth pattern: pressure increases during the injection half-cycle and decreases during the production half-cycle, with the same basic cyclic shape throughout the five-month window. However, both the upper and lower bounds of these cycles evolve gradually with time. The peak injection pressures show a mild upward trend, whereas the minimum pressures at the end of production display a more pronounced downward shift, so that each successive cycle reaches slightly higher maxima and slightly lower minima than the previous one. The resulting drift in average wellbore pressure remains moderate relative to the overall 9–12 MPa operating range, but the monotonic widening of the pressure window indicates that the system is still slowly adjusting toward a new dynamic equilibrium. Extrapolating these trends suggests that, over longer timescales, cyclic operation would continue to induce gradual but bounded changes in injectivity and productivity, rather than rapidly driving the well beyond its operational pressure envelope. This pattern is consistent with the reservoir-scale results: slow redistribution of $CO_2$ and brine and small changes in local saturation and mobility lead to incremental changes in injectivity and productivity, which are reflected in the gradual separation of the pressure peaks and troughs.

Differences between the full-length, upper-only and split completions are more evident in how the upper and lower bounds of the pressure cycles separate over time. In the full-length case, the upper envelope rises by around 0.2 MPa while the lower envelope drops by around 0.4 MPa, giving the largest widening of the cycle window. This pattern arises because production draws not only from the $CO_2$-rich caprock-proximal band but also from the brine-dominated lower half of the reservoir, and repeated withdrawal from this relatively $CO_2$-poor zone causes a gradual pressure decline at depth, while cyclic injection maintains a slight net build-up in the upper gas cap. As a result, exploiting the full 40 m interval yields the strongest long-term separation between upper and lower pressures.

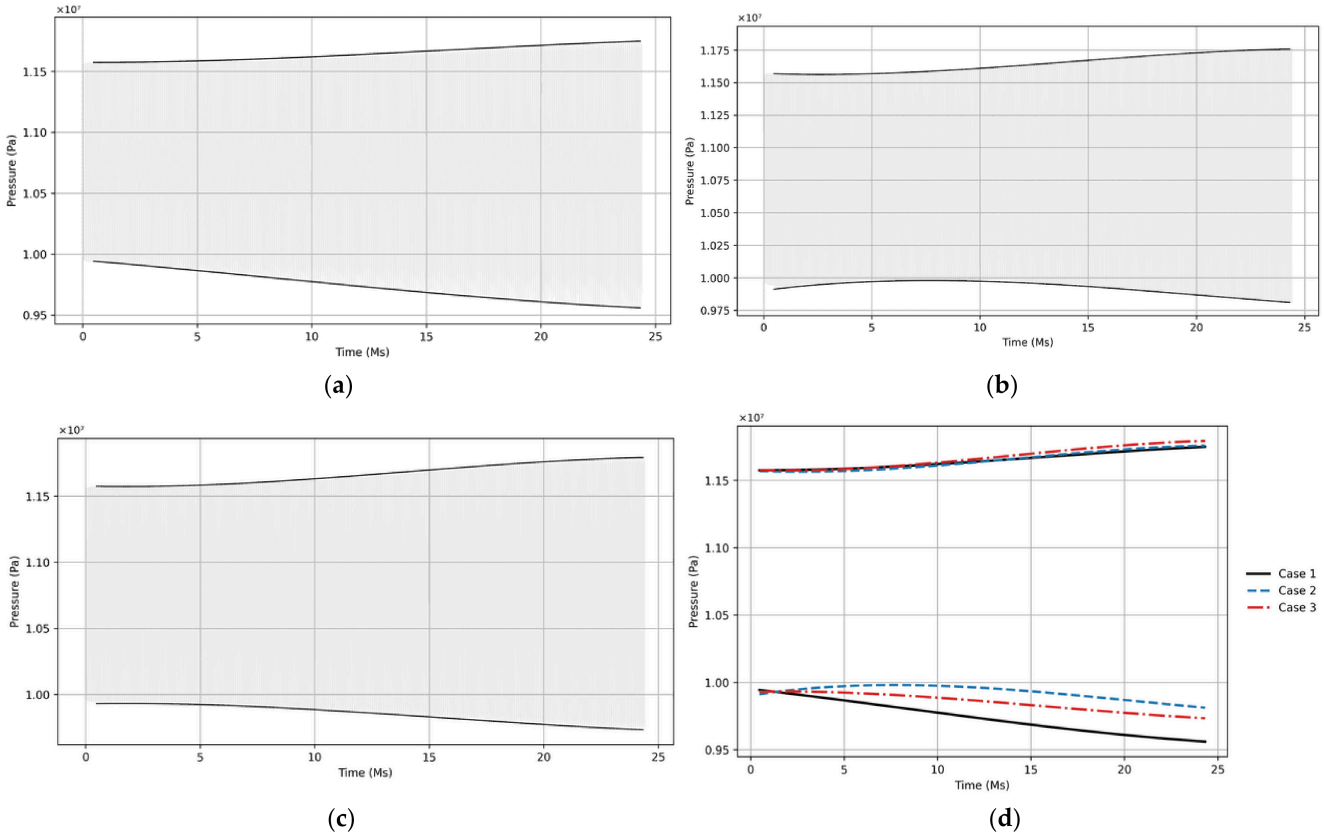


**Figure 12.** Evolution of average pressure along the perforated well interval over the 5-month refined window. Panels (**a**–**c**) show the full-length, upper-only and split-completion cases, respectively; panel (**d**) compares the three completion strategies on the same axes. For each case, the curves illustrate the gradual separation of cycle maxima and minima as cyclic operation proceeds. The high-frequency oscillations correspond to the imposed 24 h injection-production cycles; therefore, the interpretation focuses on the trend lines and the gradual separation of the upper and lower pressure envelopes.

For the upper-only completion, both envelopes move much less: the upper pressure still creeps upward by around 0.2 MPa, while the lower envelope first increases slightly and then declines only weakly, so that the net change at depth is small. The initial increase reflects transient $CO_2$ enrichment in the lower part of the completion due to $CO_2$ injection, which stiffens the local response and elevates the minimum pressure, whereas continued buoyant migration and preferential production from the upper perforations progressively bleed $CO_2$ out of this zone and allow the lower interval to relax back toward a brine-dominated state, reducing the minimum pressure. This dynamic evolution effectively damps the long-term widening of the pressure range, lowering cyclic stress amplitudes on the wellbore and adjacent rock and thus being favorable for well integrity and overall system lifetime.

The split-completion case is intermediate: the upper envelope increases by around 0.18 MPa and the lower decreases by around 0.20 MPa, so the pressure window widens less than in the full-length configuration but more than in the upper-only case. Because only part of the flow is taken from the lower half of the completion, depressurisation of the brine-rich lower interval is much slower than in the full-length case, which markedly limits the downward drift of the minimum pressure. At the same time, active withdrawal from the lower perforations accelerates the long-term loss of $CO_2$ from depth compared with the upper-only scheme, preventing the lower envelope from remaining as stable as in that configuration. As a result, both the magnitude and rate of pressure-window widening fall

between the two end-members, consistent with the split balance of flow between upper gas-rich and lower brine-buffer zones.

Overall, the pressure-envelope drift remains small relative to the absolute operating pressure. Even in the full-length case, where the widening is largest, the total envelope change is about 0.6 MPa within an operating pressure range of roughly 9–12 MPa. This indicates gradual near-well hydraulic adjustment rather than rapid pressure destabilisation. The smaller drift in the upper-only and split cases further suggests that reducing withdrawal from the lower brine-rich interval helps limit long-term pressure-window expansion.

A set of displacement maps was extracted at the end of injection and production after five months of cyclic operation for all three completion strategies to assess the geomechanical impact of CCES. As shown in Figure 13, across all completion schemes, the displacement field reflects two superposed components: a broad, gentle bending of the B salt, A-2 carbonate, and A-2 salt layers induced by the long-term pressure buildup, and a much sharper local disturbance around the well. In the end-of-injection snapshots, the dominant feature is a smooth, caprock-parallel uplift zone along the top of the A-2 carbonate directly above the $CO_2$ wedge, extending laterally well beyond the refined near-well region. Superimposed on this are small vertical kinks near the reservoir-caprock contacts and a modest local bulge around the wellbore, consistent with injection-induced overpressure concentrated in the upper part of the reservoir. This observed pattern reflects poroelastic coupling: elevated pore pressure within the $CO_2$-rich upper A-2 carbonate reduces effective vertical stress, causing slight expansion of the reservoir layer and flexural uplift of the overlying B salt, while contrasts in stiffness at the carbonate-salt interfaces localise vertical strain into the observed kinks. In addition, the localized bulge around the wellbore is attributed to the largest pore-pressure gradients occurring in the near-well region during injection.

At the end of production, the far-field bending nearly relaxes back toward the pre-injection state and the remaining deformation is much more localized: a small, symmetric compaction bowl develops around the well, affecting mainly the upper A-2 carbonate and the immediately over- and underlying salt, while the outer parts of the model show almost no visible change. This response is again poroelastic in origin: pressure drawdown in the near-well region increases effective stress in the $CO_2$-charged interval, leading to slight vertical shortening of the reservoir and downward deflection of the overlying B salt. Because the pressure perturbation decays rapidly with distance and the surrounding halite is comparatively stiff and tight, this compaction is confined to a narrow zone around the well, and the far-field stress and displacement fields remain essentially unchanged.

Differences between the three completion schemes are expressed mainly in the amplitude and vertical reach of the near-well deformation bowl. In the full-length completion, both the end-of-injection uplift and end-of-production compaction are most pronounced: the displacement anomaly extends through nearly the entire 40 m reservoir interval and into the adjacent B-salt and A-2 salt, and peak magnitudes around the wellbore are largest among the three cases. This is consistent with the pressure and saturation results, where the full interval is actively cycled and the brine-dominated lower zone experiences the strongest long-term pressure decline. In the upper-only case, by contrast, deformation is tightly concentrated in the upper part of the A-2 carbonate and the base of the B-salt, with only very weak displacements in the lower reservoir and underlying salt. The compaction bowl around the well is shallower and has the smallest amplitude, reflecting that the lower half of the reservoir mainly acts as a buffered brine zone with limited direct participation in the cycles. The split completion shows an intermediate response: the deformation bowl penetrates deeper than in the upper-only case but remains less developed than in the full-length configuration, mirroring the fact that only part of the flow is drawn from the lower interval while the upper gas-rich zone still dominates the cyclic pressure changes.

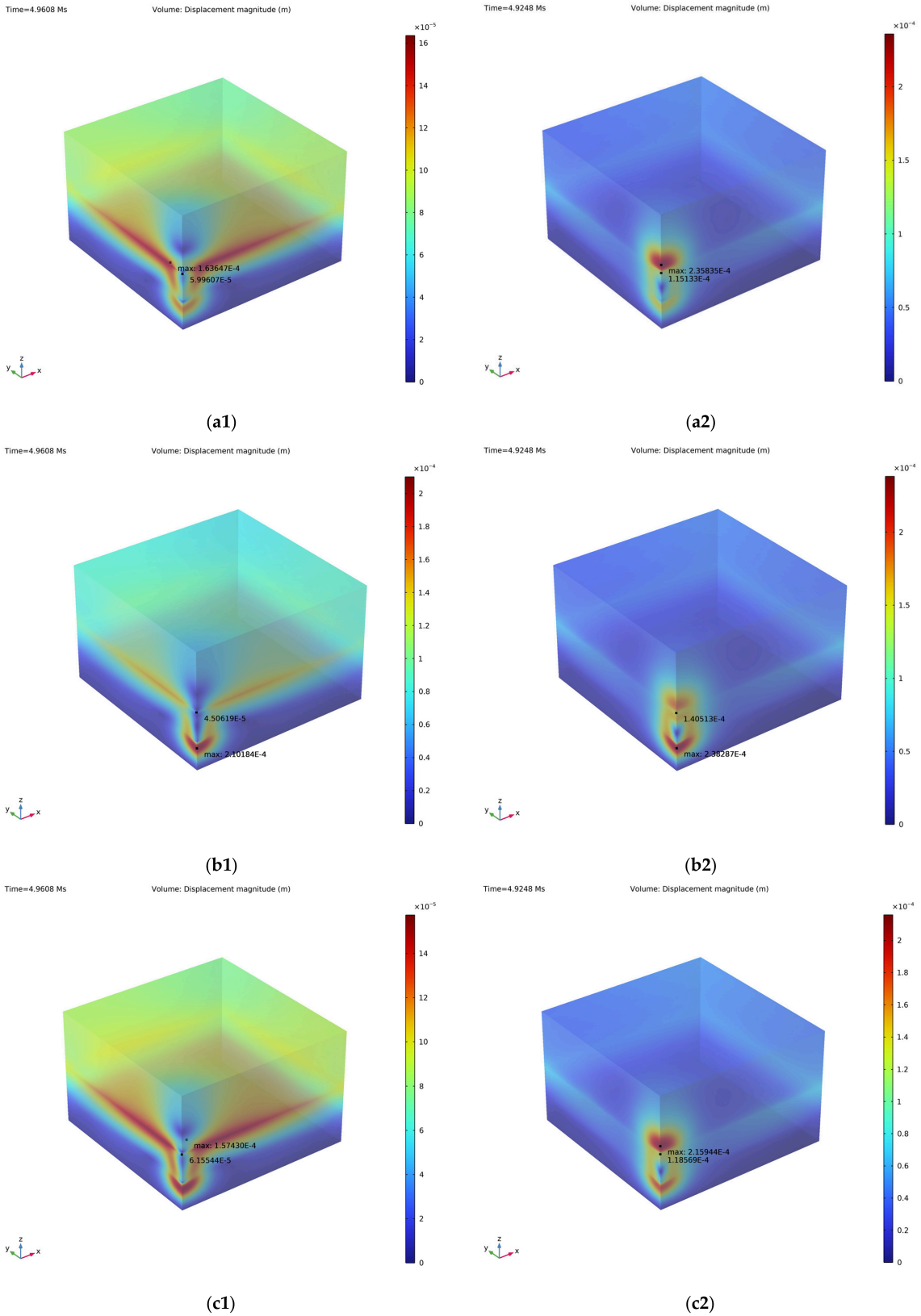


**Figure 13.** Displacement fields after five months of timestep refined cyclic operation for the three completion strategies. Panels (**a**–**c**) correspond to full-length completion, half-length completion, split-length completion respectively. For each pair of panels, the left plot shows the displacement field at the end of an injection half-cycle, and the right plot shows the corresponding field at the end of the subsequent production half-cycle.

In all simulations, peak displacements remain small, on the order of $10^{-4}$–$10^{-3}$ m. These values are several orders of magnitude smaller than the Salina unit thicknesses and correspond to incremental strains of approximately $10^{-7}$–$10^{-6}$. The associated changes in principal stresses are therefore very small compared with the in situ stress magnitudes and rock strengths. Because these stress perturbations closely follow the spatial pattern of the displacements and remain negligible at the scale of the basin stratigraphy, detailed stress contour plots are not presented; instead, the geomechanical response is summarised using the displacement fields as a compact proxy for the small perturbation to the stress field.

## 6. Discussion

This study aimed to evaluate whether a Salina Group A-2 carbonate interval bounded by B and A-2 salts beneath offshore Lake Huron can serve as a viable porous-medium host for compressed $CO_2$ energy storage, and how alternative well completions modify plume evolution, $CO_2$ deliverability and coupled hydraulic-mechanical responses under a realistic basin-scale depth and stress regime. The simulations indicate that the B–A-2 system beneath offshore Lake Huron can, in principle, support cyclic compressed $CO_2$ energy storage with limited hydraulic and mechanical disturbance. After an initial cushion-gas phase, the $CO_2$ plume rapidly organises into a caprock-parallel wedge pinned beneath the B-salt, with high saturation in the upper 10–15 m and a brine-dominated lower interval. Subsequent cushion injection mainly thickens and extends this upper gas cap, while the lower A-2 carbonate evolves into a weak $CO_2$ source and a pressure buffer. From an operational standpoint, this implies that once a laterally continuous gas wedge is established, further cushion injection yields diminishing returns for CCES: additional $CO_2$ is stored at the far leading edge, where it contributes little to daily cycling. These results suggest a broader implication for porous-media CCES in evaporite-confined carbonate reservoirs: once a continuous $CO_2$-rich layer is established beneath the upper seal, system performance is controlled mainly by buoyancy-driven vertical segregation and completion-dependent working-volume distribution. Completion design therefore provides a practical means to balance $CO_2$ deliverability against pressure-window widening and near-well deformation.

On this background, all three completion strategies preserve a robust plume architecture over two years of 24 h cycling plus the refined five-month window. Cyclic operation mainly breathes the near-well region while maintaining a continuous gas cap along the B-salt, so that the system behaves like a mature gas-storage reservoir as $CO_2$ production stays high with only weak decline, and saturation changes remain concentrated in the caprock-proximal wedge with limited additional depletion at depth. Pore pressure and displacement results are consistent with this picture: far-field pressures stay close to hydrostatic, the widening of the local pressure window at the well remains modest within a 9–12 MPa band, and deformations are restricted to sub-millimetre uplift and compaction around the well. These small strains imply only minor perturbations of the in situ stress field and indicate a substantial geomechanical safety margin under the simulated operating conditions.

Within this generally stable response, completion design mainly controls the balance between storage-volume utilisation, $CO_2$ deliverability and long-term pressure behavior. Full-length completion mobilises the entire 40 m interval and gives the broadest depletion footprint and widest lateral $CO_2$ spread, but at the price of the lowest $CO_2$ production rate, the strongest depressurisation of the lower brine-rich zone, and the largest widening of the wellbore pressure window and deformation bowl. Upper-only completion is the opposite: it delivers the highest and most $CO_2$-rich production, keeps the plume comparatively compact and minimises changes in lower-reservoir pressure and deformation, but it relies on a thinner effective working volume and shows a slightly steeper relative production decline.

In addition, concentrating flow into the upper half of the interval also increases the average flux per metre of perforation, implying higher local loading on the wellbore and completion compared with the other schemes. The split completion offers a compromise by drawing from both upper and lower halves at different rates, engaging more storage thickness than the upper-only scheme without inducing the strong lower-zone pressure drop seen in the full-length case. Consequently, it maintains a high and stable $CO_2$ production rate, limits the growth of the pressure window and deformation to intermediate levels, and preserves a robust gas cap whose extent and saturation lie between the two end-members. Given that the absolute differences remain modest over the simulated period, the Salina B–A-2 system appears flexible, and split completion emerges as a practical balance between deliverability and long-term hydraulic-mechanical performance.

Several limitations of the present work should be acknowledged. The geological model is idealised as laterally homogeneous, with simple, flat layering; real Salina successions show thickness variations and local structural features that could alter plume pathways, pressure communication and caprock performance. Flow physics are simplified: hysteresis and $CO_2$ dissolution and reactive transport are treated in a reduced form, and the chosen permeability for the A-2 carbonate implicitly assumes some degree of reservoir pre-treatment. Mechanically, the rock is treated as linear, isotropic poroelastic; therefore, time-dependent salt creep, plasticity, damage and faulting are neglected, so long-term visco-plastic relaxation and potential failure modes cannot be evaluated. The simulations also consider a single well in a finite domain with an idealised daily duty cycle; multi-well interference, regional boundary effects, and more complex operational patterns like seasonal net injection, shut-in periods, variable rates remain unexplored. Direct model validation is also not possible at present because no CCES project has yet been implemented in the Salina Group beneath offshore Lake Huron. Accordingly, this work should be viewed as a first-order assessment of feasibility and relative completion performance in a representative B–A-2 setting, rather than as a site-specific design study. Subsequent study will stress these limitations by introducing stratigraphic heterogeneity, more detailed multiphase and geochemical processes, visco-plastic salt behavior, multi-well configurations and alternative operational schedules to test the robustness of the present conclusions. Future work should also incorporate site-specific heterogeneity, explicit leakage pathways, more detailed well and caprock representations, multi-well scenarios, and stronger validation. Possible validation pathways include laboratory measurements of Salina carbonate and salt properties, benchmarking against established reservoir simulators or analytical pressure-transient solutions, and calibration against monitoring data from future pilot-scale $CO_2$ injection or CCES tests. Nonetheless, within the controlled scenario considered here, the results indicate that a Salina Group A-2 carbonate reservoir bounded by B and A-2 salts beneath Lake Huron can host cyclic compressed $CO_2$ energy storage with only modest pressure and deformation responses, and that carefully chosen completions—particularly split designs—can enhance $CO_2$ deliverability while keeping hydraulic and mechanical impacts within an operationally acceptable range. Although the specific pressure, saturation, and deformation values are site-dependent, the controlling mechanisms identified here are relevant to other sealed porous reservoirs, particularly where a permeable storage interval is bounded by low-permeability confining units. For formations with different permeability, thickness, depth, or seal properties, the same modelling framework can be adapted by recalibrating the geological, hydraulic, thermal, and mechanical parameters.

**Author Contributions:** Writing, J.H. and Y.C.; supervision, S.Y. and J.W. All authors have read and agreed to the published version of the manuscript.

**Funding:** This research received no external funding.

**Data Availability Statement:** The data that support the findings of this study are available from the co-authors upon request due to privacy issues.

**Conflicts of Interest:** Jennifer Williams is employed by the company Newfoundland and Labrador Hydro (NL Hydro). The remaining authors declare that the research was conducted in the absence of any commercial or financial relationships that could be construed as a potential conflict of interest.

## References


1. Myhre, G.; Shindell, D.; Bréon, F.-M.; Collins, W.; Fuglestvedt, J.; Huang, J.; Koch, D.; Lamarque, J.-F.; Lee, D.; Mendoza, B.; et al. *Anthropogenic and Natural Radiative Forcing. Climate Change 2013: The Physical Science Basis*; Cambridge University Press: Cambridge, UK; New York, NY, USA, 2014; pp. 659–740. [CrossRef]
2. Friedlingstein, P.; O'Sullivan, M.; Jones, M.W.; Andrew, R.M.; Hauck, J.; Landschützer, P.; Le Quéré, C.; Li, H.; Luijkx, I.T.; Olsen, A.; et al. Global Carbon Budget 2024. *Earth Syst. Sci. Data* **2025**, *17*, 965–1039. [CrossRef]
3. Masson-Delmotte, V.; Zhai, P.; Pirani, A.; Connors, S.L.; Péan, C.; Berger, S.; Caud, N.; Chen, Y.; Goldfarb, L.; Gomis, M.I. (Eds.) *Climate Change 2021: The Physical Science Basis. Contribution of Working Group I to the Sixth Assessment Report of the Intergovernmental Panel on Climate Change*; Cambridge University Press: Cambridge, UK; New York, NY, USA, 2021.
4. Rogelj, J.; Popp, A.; Calvin, K.V.; Luderer, G.; Emmerling, J.; Gernaat, D.; Fujimori, S.; Strefler, J.; Hasegawa, T.; Marangoni, G.; et al. Scenarios towards Limiting Global Mean Temperature Increase below 1.5 °C. *Nat. Clim. Change* **2018**, *8*, 325–332. [CrossRef]
5. Antonietti, R.; Fontini, F. Does Energy Price Affect Energy Efficiency? Cross-Country Panel Evidence. *Energy Policy* **2019**, *129*, 896–906. [CrossRef]
6. Grubler, A.; Wilson, C.; Bento, N.; Boza-Kiss, B.; Krey, V.; McCollum, D.L.; Rao, N.D.; Riahi, K.; Rogelj, J.; De Stercke, S.; et al. A Low Energy Demand Scenario for Meeting the 1.5 °C Target and Sustainable Development Goals without Negative Emission Technologies. *Nat. Energy* **2018**, *3*, 515–527. [CrossRef]
7. Ringrose, P.S.; Furre, A.-K.; Gilfillan, S.M.V.; Krevor, S.; Landrø, M.; Leslie, R.; Meckel, T.; Nazarian, B.; Zahid, A. Storage of Carbon Dioxide in Saline Aquifers: Physicochemical Processes, Key Constraints, and Scale-Up Potential. *Annu. Rev. Chem. Biomol. Eng.* **2021**, *12*, 471–494. [CrossRef]
8. Heinemann, N.; Alcalde, J.; Miocic, J.M.; Hangx, S.J.T.; Kallmeyer, J.; Ostertag-Henning, C.; Hassanpouryouzband, A.; Thaysen, E.M.; Strobel, G.J.; Schmidt-Hattenberger, C.; et al. Enabling Large-Scale Hydrogen Storage in Porous Media—The Scientific Challenges. *Energy Environ. Sci.* **2021**, *14*, 853–864. [CrossRef]
9. Creutzig, F.; Agoston, P.; Goldschmidt, J.C.; Luderer, G.; Nemet, G.; Pietzcker, R.C. The Underestimated Potential of Solar Energy to Mitigate Climate Change. *Nat. Energy* **2017**, *2*, 17140. [CrossRef]
10. Net-Zero Emissions Energy Systems on JSTOR. Available online: https://www-jstor-org.proxy.lib.uwaterloo.ca/stable/26498428 (accessed on 6 February 2026).
11. Brown, T.; Schlachtberger, D.; Kies, A.; Schramm, S.; Greiner, M. Synergies of Sector Coupling and Transmission Reinforcement in a Cost-Optimised, Highly Renewable European Energy System. *Energy* **2018**, *160*, 720–739. [CrossRef]
12. Sepulveda, N.A.; Jenkins, J.D.; de Sisternes, F.J.; Lester, R.K. The Role of Firm Low-Carbon Electricity Resources in Deep Decarbonization of Power Generation. *Joule* **2018**, *2*, 2403–2420. [CrossRef]
13. Luderer, G.; Madeddu, S.; Merfort, L.; Ueckerdt, F.; Pehl, M.; Pietzcker, R.; Rottoli, M.; Schreyer, F.; Bauer, N.; Baumstark, L.; et al. Impact of Declining Renewable Energy Costs on Electrification in Low-Emission Scenarios. *Nat. Energy* **2022**, *7*, 32–42. [CrossRef]
14. Schmidt, O.; Melchior, S.; Hawkes, A.; Staffell, I. Projecting the Future Levelized Cost of Electricity Storage Technologies. *Joule* **2019**, *3*, 81–100. [CrossRef]
15. Budt, M.; Wolf, D.; Span, R.; Yan, J. A Review on Compressed Air Energy Storage: Basic Principles, Past Milestones and Recent Developments. *Appl. Energy* **2016**, *170*, 250–268. [CrossRef]
16. Liu, H.; He, Q.; Borgia, A.; Pan, L.; Oldenburg, C.M. Thermodynamic Analysis of a Compressed Carbon Dioxide Energy Storage System Using Two Saline Aquifers at Different Depths as Storage Reservoirs. *Energy Convers. Manag.* **2016**, *127*, 149–159. [CrossRef]
17. Liu, Z.; Yan, X.; Wang, S.; Wei, X.; Zhang, Y.; Ding, J.; Su, C. Performance of Compressed $CO_2$ Energy Storage Systems with Different Liquefaction and Storage Scenarios. *Fuel* **2024**, *359*, 130527. [CrossRef]
18. Pruess, K. Enhanced Geothermal Systems (EGS) Using $CO_2$ as Working Fluid—A Novel Approach for Generating Renewable Energy with Simultaneous Sequestration of Carbon. *Geothermics* **2006**, *35*, 351–367. [CrossRef]
19. Randolph, J.B.; Saar, M.O. Combining Geothermal Energy Capture with Geologic Carbon Dioxide Sequestration. *Geophys. Res. Lett.* **2011**, *38*, L10401. [CrossRef]
20. Fotias, S.P.; Bellas, S.; Gaganis, V. Optimizing Geothermal Energy Extraction in $CO_2$ Plume Geothermal Systems. *Mater. Proc.* **2023**, *15*, 52. [CrossRef]

21. Caruthers, A.H.; Gröcke, D.R.; Kaczmarek, S.E.; Rine, M.J.; Kuglitsch, J.; Harrison, W.B., III. Utility of Organic Carbon Isotope Data from the Salina Group Halite (Michigan Basin): A New Tool for Stratigraphic Correlation and Paleoclimate Proxy Resource. *GSA Bull.* **2018**, *130*, 1782–1790. [CrossRef]
22. Perry, F.V.; Kelley, R.E.; Dobson, P.F. *Regional Geology: Distribution of Alternative Host Rock Formations and Description of Siting Factors That Potentially Influence Siting and Site Characterization Activities*; Report No. M3FT-12LA0807011; Los Alamos National Laboratory: Los Alamos, NM, USA; Lawrence Berkeley National Laboratory: Berkeley, CA, USA, 2012. Available online: https://curie.pnnl.gov/sites/default/files/sandiadocs/M3FT-12LA0807011-Regional-Geology-Distribution-of-Alternative-Host-Rock-Formations-and-Description-of-Siting-Factors-th.pdf (accessed on 7 February 2026).
23. Hydrologic Environment of the Silurian Salt Deposits in Parts of Michigan, Ohio, and New York | U.S. Geological Survey. Available online: https://www.usgs.gov/publications/hydrologic-environment-silurian-salt-deposits-parts-michigan-ohio-and-new-york (accessed on 7 February 2026).
24. Carter, T.; Fortner, L.; Russell, H.; Skuce, M.; Longstaffe, F.; Sun, S. A Hydrostratigraphic Framework for the Paleozoic Bedrock of Southern Ontario. *Geosci. Can.* **2021**, *48*, 23–58. [CrossRef]
25. Rine, M.J.; McLaughlin, P.I.; Bancroft, A.M.; Harrison, W.B.; Kuglitsch, J.; Caruthers, A.H.; Ramezani, J.; Kaczmarek, S.E.; Emsbo, P. Linked Silurian Carbon Cycle Perturbations, Bursts of Pinnacle Reef Growth, Extreme Sea-Level Oscillations, and Evaporite Deposition (Michigan Basin, USA). *Palaeogeogr. Palaeoclimatol. Palaeoecol.* **2020**, *554*, 109806. [CrossRef]
26. Tomastik, T.E. The Sedimentology of the Bass Islands and Salina Groups in Ohio and Its Effect on Salt-Solution Mining and Underground Storage, USA. *Carbonates Evaporites* **1997**, *12*, 236–253. [CrossRef]
27. Li, L.; Yin, S.; Wang, Z. A Preliminary Assessment of Underground Space Resources for Hydrogen Storage in Salt Caverns in Lambton County, Southern Ontario, Canada. *Mining* **2024**, *4*, 530–545. [CrossRef]
28. Hewitt, D.F. *Salt in Ontario*; Industrial Mineral Report No. 6; Ontario Department of Mines: Toronto, ON, Canada, 1962; 37p. Available online: https://prd-0420-geoontario-0000-blob-cge0eud7azhvfsf7.z01.azurefd.net/lrc-geology-documents/publication/IMR006/IMR006.pdf (accessed on 7 February 2026).
29. Biot, M.A. Theory of elasticity and consolidation for a porous anisotropic solid. *J. Appl. Phys.* **1955**, *26*, 182–185. [CrossRef]
30. NWMO and AECOM Canada Ltd. Regional Geology—Southern Ontario. Nuclear Waste Management Organization Report NWMO DGR-TR-2011-11 R000, Toronto, Canada. 2011. Available online: https://archive.opg.com/pdf_archive/Deep%20Geologic%20Repository%20Documents/Geoscience%20Reports/D004_4.1.4_Regional-Geology---Southern-Ontario.pdf (accessed on 7 February 2026).
31. Metz, B.; Davidson, O.; de Coninck, H.C.; Loos, M.; Meyer, L.A. Underground Geological Storage. In *IPCC Special Report on Carbon Dioxide Capture and Storage*; Intergovernmental Panel on Climate Change, Cambridge University Press: Cambridge, UK; New York, NY, USA, 2005; pp. 195–276.
32. Liu, W.; Muhammad, N.; Chen, J.; Spiers, C.J.; Peach, C.J.; Deyi, J.; Li, Y. Investigation on the Permeability Characteristics of Bedded Salt Rocks and the Tightness of Natural Gas Caverns in Such Formations. *J. Nat. Gas. Sci. Eng.* **2016**, *35*, 468–482. [CrossRef]
33. Bedded Salt in Ontario: Geology, Solution Mining and Cavern Storage. Available online: https://www.ogsrlibrary.com/downloads/Salt-Geology-and-Cavern-Storage-OPI-2009.pdf (accessed on 7 February 2026).
34. Hui, S.; Yin, S.; Pang, X.; Chen, Z.; Shi, K. Potential of Salt Caverns for Hydrogen Storage in Southern Ontario, Canada. *Mining* **2023**, *3*, 399–408. [CrossRef]
35. Shahmohammadi, M.; Jafarpour, B.; Tchelepi, H.A. Data-Driven Modeling and Optimization of $CO_2$ Geological Storage Using Reduced-Order Models. In Proceedings of the Stanford Geothermal Workshop 2019, Stanford University, Stanford, CA, USA, 11–13 February 2019.
36. Sykes, J.F.; Normani, S.D.; Yin, Y. Hydrogeologic Modeling in Support of Ontario Power Generation's Proposed Deep Geologic Repository for Low and Intermediate Level Radioactive Waste, Tiverton, Ontario. In Proceedings of the GeoCanada 2010—Working with the Earth, Calgary, AB, Canada, 10–14 May 2010.


**Disclaimer/Publisher's Note:** The statements, opinions and data contained in all publications are solely those of the individual author(s) and contributor(s) and not of MDPI and/or the editor(s). MDPI and/or the editor(s) disclaim responsibility for any injury to people or property resulting from any ideas, methods, instructions or products referred to in the content.